Ore Geology Reviews 155 (2023) 105359

Contents lists available at ScienceDirect

Ore Geology Reviews

journal homepage: www.elsevier.com/locate/oregeorev

Wolframite geochronology and scheelite geochemistry of the Yangwuchang W-Au deposit and Dashegou W deposit in the Yangxie ore district, the North Qinling, China: Implications for W-Au mineralization

Jize Li [a], Jiajun Liu [a,*], Jeffrey de Fourestier [b], Degao Zhai [a], Di Hao [c], Zhanlin Ge [c], Yanwen Tang [d], Fangfang Zhang [a], Yinhong Wang [a], Jianping Wang [a]

[a] State Key Laboratory of Geological Processes and Mineral Resources, School of Earth Sciences and Resources, China University of Geosciences, Beijing 100083, PR China
[b] State Key Laboratory of Nuclear Resources and Environment, East China University of Technology, Nanchang 330013, PR China
[c] Xi'an Center of Mineral Resources Survey, China Geological Survey, Xi'an 710100, PR China
[d] State Key Laboratory of Ore Deposit Geochemistry, Institute of Geochemistry, Chinese Academy of Sciences, Guiyang 550081, PR China

ARTICLE INFO

Keywords:
Scheelite
Cathodoluminescence
Trace element
Wolframite in-situ U-Pb dating
Yangwuchang W-Au deposit
Dashegou W deposit

ABSTRACT

The characteristics of W-Au mineralization have received great attention, however still under debate. The Yangwuchang W-Au deposit and Dashegou W deposit are two newly discovered quartz-vein type deposits in the Yangxie Au-W ore district, the North Qinling Orogenic Belt, China. The characteristics of W-Au mineralization in these deposits remain poorly understood. Hence, in order to determine the mineralization timing and its genetic link with magmatism, as well as the source, nature, and evolution of the ore-forming fluids, we undertook a combined study of wolframite geochronology with scheelite texture and geochemistry. In-situ U-Pb dating of wolframite shows that the timing of W mineralization is 141.8–139.1 Ma. This age range is perfectly matched with the published Au metallogenic age in the ore district. Hence, the W-Au mineralization should be associated with Early-Cretaceous magmatism, ruling out the genetic relationship with the Late-Triassic magmatism. Based on cathodoluminescence (CL) imaging and in-situ trace elements analyses, two generations of scheelite (Sch-I and Sch-II) can be discriminated. The CL images of Sch-I show a weak intensity, distinct boundary, and zonation pattern. In contrast, Sch-II is characterized by a bright and homogeneous CL response that encloses or crosscuts Sch-I. Sch-I shows depletion in Mo, Mn, Nb, and Y, and slight enrichment in Sr and U. It is also characterized by MREE-depleted chondrite-normalized patterns with strongly positive Eu anomalies. Compared with Sch-I, Sch-II has elevated concentrations of trace elements and MREE-enriched patterns with slightly positive Eu anomalies. The changes of MREEs, Y, and Mn contents are the main factor causing the CL intensity difference. Our data reveals that $3Ca^{2+} = (2REE)^{3+} + {}_{\square}Ca$ (site vacancy) is the main substitution mechanism that controls REEs into the scheelite. The strong positive Eu anomalies of Sch-I in the Yangwuchang deposit are related to the Eu^{2+} released from plagioclase in the country rock during greisenization. Other Eu anomalies of Sch-I and Sch-II were inherited from ore-forming fluids. The positive Eu anomalies and low contents of Mo and As point out a strongly reduced environment. The geochemical features of scheelite decipher that the ore-forming fluids of the Yangwuchang W-Au deposit and Dashegou W deposit were single-derived reduced magmatic fluids. The decomposition of plagioclase in the host rocks provided significant Ca for scheelite precipitation. The cooling and depressurization of W-Au-rich magmatic fluids may be the main mechanism accounting for W-Au mineralization.

1. Introduction

Tungsten mineralization is dominated by greisen, skarn, porphyry, quartz-vein, and metamorphic types (Ghaderi et al., 1999; Wood and Samson, 2000; Brugger et al., 2002; Dostal et al., 2009; Poulin et al., 2018; Wang et al., 2022; Li et al., 2022). In addition, tungsten minerals also can coexist with gold in different types of deposits, ranging from the orogenic deposit (e.g. the Mt. Charlotte W-Au deposit, Australia;

* Corresponding author.
E-mail address: liujiajun@cugb.edu.cn (J. Liu).

https://doi.org/10.1016/j.oregeorev.2023.105359
Received 12 October 2022; Received in revised form 19 January 2023; Accepted 17 February 2023
Available online 20 February 2023

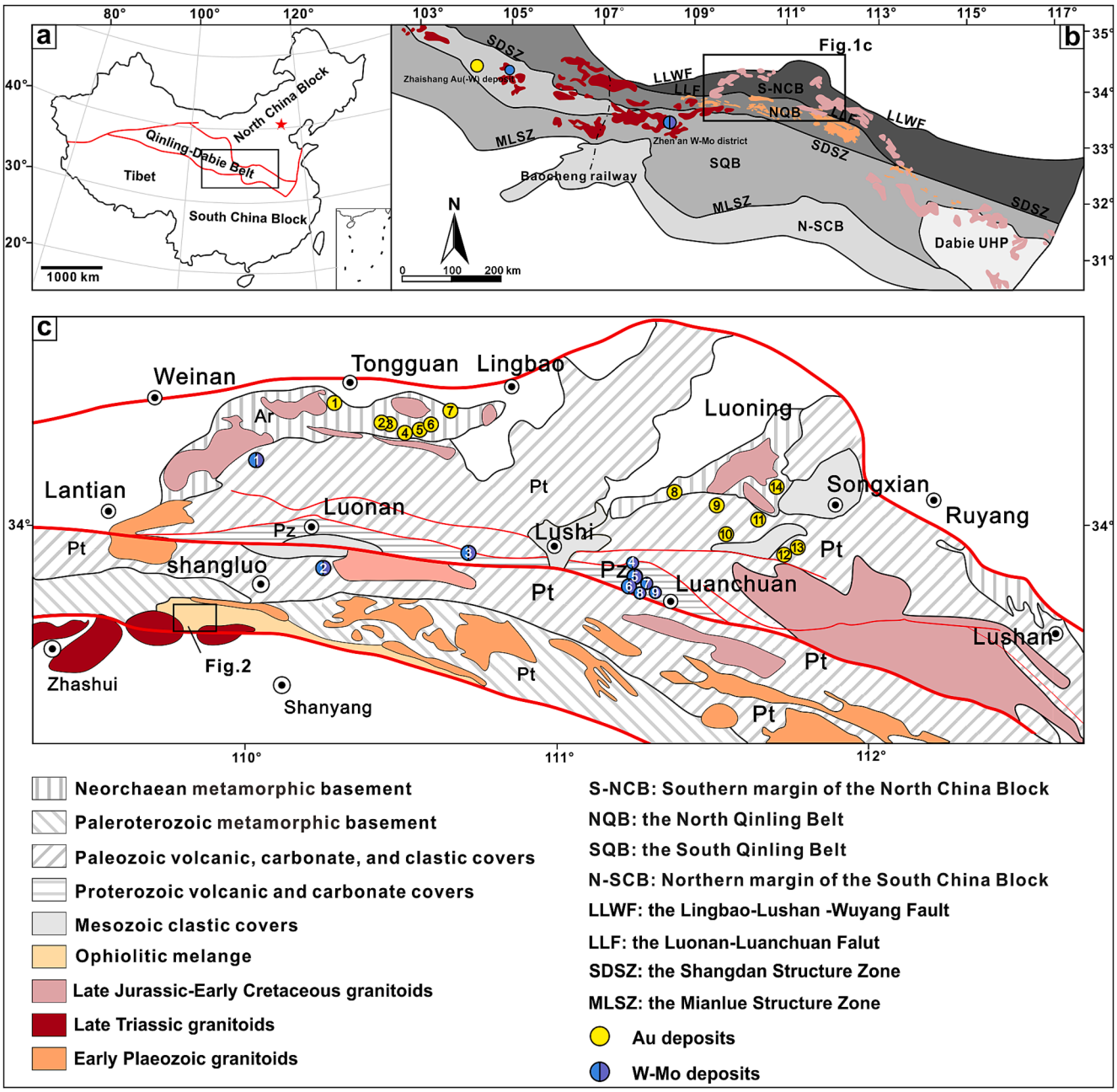

Fig. 1. Simplified tectonic map of the Qinling Orogenic Belt (QOB) with the distribution of intrusions, W and Au deposits, and the location of the Yangxie W-Au ore district. Gold deposits 1)-14): Tongguan, Wenyu, Dongchuang, Qiangma, Yangzhaiyu, Tonggou, Dahu, Shanggong, Huanxiangwa, Beiling, Huashuping, Qianhe, Miaoling, Leimengou. W-Mo deposits 1)-9): Jinduicheng, Nantai, Yechangping, Majuan, Nannihu-Sandaozhuang, Shangfanggou, Zhazigou; Dongyuku; Jiudinggou (Collected from Mao et al., 2011; Li et al., 2013; Liu et al., 2015; Zhao er al., 2018 Yin et al., 2019).

Brugger et al., 2002), vein-type deposit (e.g. the Xiangdong and Goudalan deposits, China; Liu et al., 2019), skarn deposit (e.g. the Bonfim W-Au deposit, Brazil; Neto et al., 2008), carlin-like deposit (e.g. the Zhaishang Au-(W) deposit, China; Liu et al., 2015) and reduced intrusion-related gold systems (e.g. the Bjorkdal Au-W deposit, Sweden; Roberts et al., 2006). The deposits with the W-Au association have widely occurred throughout the world, however, few have extensive mineralization to form a W-Au metallogenic belt. The W and Au could have paragenesis, but they also could show differentiation at different scales. In the metallogenic belt hosts W-Au deposit, it also could distribute a large amount of Au deposit and W deposit separately, and other deposits with multi-element assemblage such as Au-Sb, Au-Bi, W-Mo, W-Sn, Cu-W, W-Mo-Cu-Au, etc. For example, the Xuefengshan metallogenic belt host the Woxi Au-Sb-W deposit, the Longshan Au-Sb-W deposit, the Xi'an W deposit, as well as the Chanziping Au deposit (Gu et al., 2007; Zhang et al., 2019; Zhang et al., 2020); the xiaoqinling Au metallogenic belt host the Dahu Au-W deposit (Yin et al., 2019). Up to now, previous studies on the W-Au association deposits are mainly focused on the mineralization characteristics, metallogenic ages (e.g. Guo et al., 2016), physicochemical condition (e.g. Kovalenker et al., 2019), and source of ore-forming fluids and materials (e.g. Zhang et al., 2019). However, the mechanism of W-Au paragenesis and differentiation is still unclear.

With the advances of in-situ laser-ablation inductively-coupled-plasma mass spectrometry (LA-ICP-MS) technology, the trace element compositions of scheelite ($CaWO_4$) have been widely used as a powerful tool for deposit studies, including not only W deposits but also other metals deposits such as Au, Cu, Mo, and Sn (Ghaderi et al., 1999; Song

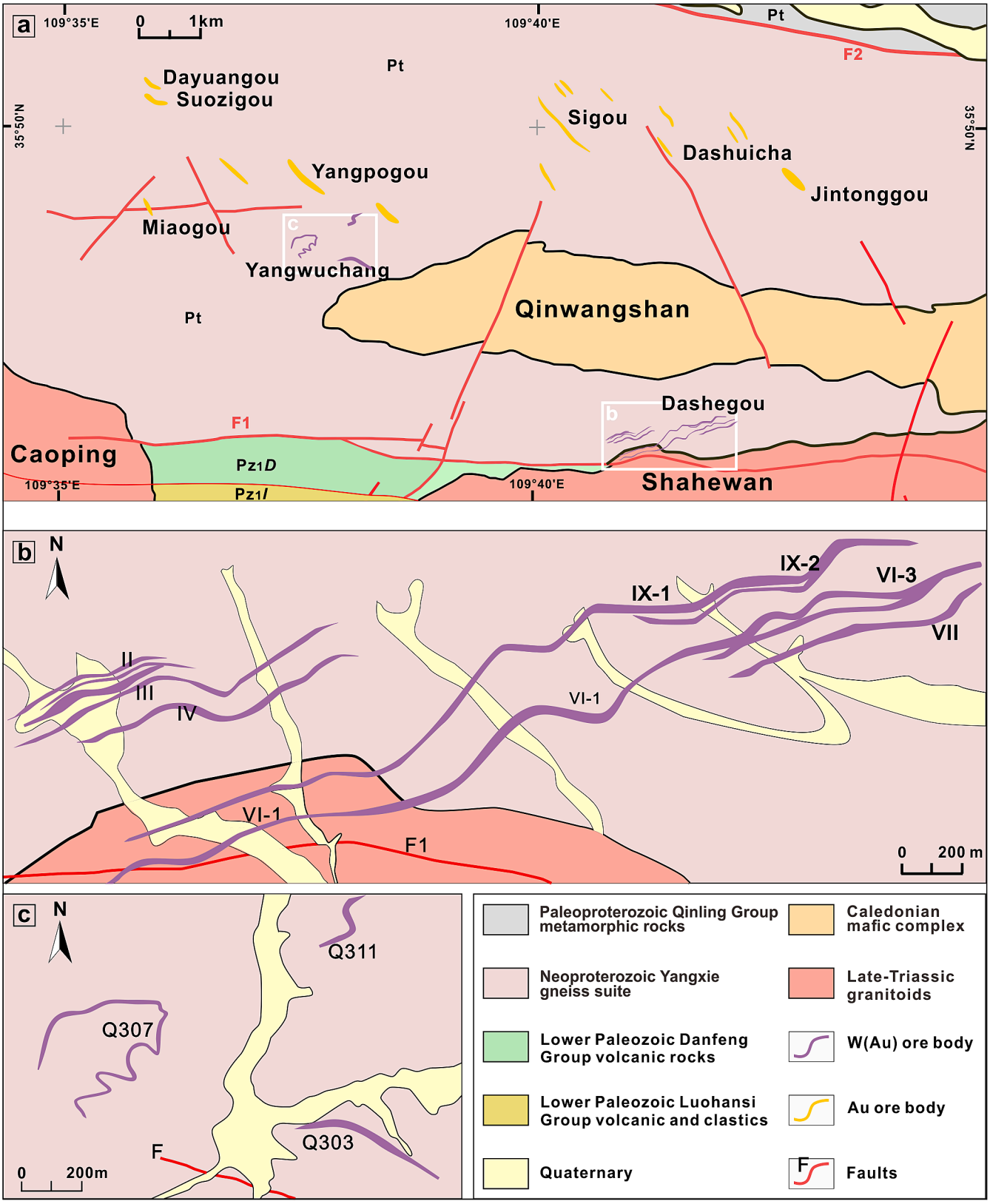

Fig. 2. (a) Sketch geological map of the Yangxie W-Au ore district. (b) Sketch geological map of the Dashegou W deposit. (c) Sketch geological map of the Yangwuchang W-Au deposit. Modified after (Ge et al., 2020, 2021).

et al., 2014; Dai et al., 2022; Miranda et al., 2022). Due to similar electron configurations and ionic radii, scheelite can concentrate abundant trace elements by substitution with Ca^{2+} or W^{6+}, such as REEs, Sr, Y, Mo (Nassau and Loiacono, 1963; Burt, 1989; Ghaderi et al., 1999; Brugger et al., 2000b; MacRae et al., 2009; Poulin et al., 2016, 2018; Miranda et al., 2022; Xiao et al., 2022). Redox-sensitive elements like Eu, Mo, and As can record the redox state of the ore-forming fluids by their variable valence states (Song et al., 2014; Sun and Chen, 2017; Poulin et al., 2018; Han et al., 2020). In addition, indicative elements such as Y and Ho could also infer the fluid chemistry and mineralization process (Bau and Möller, 1992; Dostal et al., 2009; Li et al., 2019; Liu et al., 2019). The REEs and trace elements can be used to discriminate different mineralized settings (Song et al., 2014; Poulin et al., 2018; Liu et al., 2021b). However, scheelite generally undergoes multi-generation mineralization or hydrothermal modification, which will complicate or mislead geochemical interpretation (Su et al., 2019; Han et al., 2020). Cathodoluminescence (CL) is useful in revealing inner textures, crystal growth, and chemical distributions that are hard to observe using a conventional light microscope (Brugger et al., 2000a; Götze et al., 2001; Müller et al., 2010; Poulin et al., 2016). These internal textures provide vital information for the reconstruction of geological processes or the characterization of technical products (Wang et al., 2022). It has been widely used in numerous petrological studies of minerals from various geological environments, including quartz, apatite, carbonate, and scheelite as well (Frelinger et al., 2015; Wang et al., 2022). Hence, scheelite can provide significant information on the source, nature, and evolution of ore-forming fluids, physicochemical conditions of ore formation, genetic types of deposits, mineralization processes, and so on (Ghaderi et al., 1999; Brugger et al., 2002; Song et al., 2014; Sun and Chen, 2017; Poulin et al., 2018; Han et al., 2020; Sciuba et al., 2020; Li et al., 2021; Dai et al., 2022).

Tungsten deposits are temporally, spatially, and genetically associated with granitoids in major deposit settings (Korges et al., 2018; Yuan et al., 2019). Therefore, metallogenic age determination is an indispensable part of W deposit studies. It is critical to link the W mineralization with regional magmatic processes (Tang et al., 2020; Yang et al., 2020). Generally, scheelite Sm-Nd dating and accessory minerals dating, such as molybdenite Re-Os dating, Zircon, and cassiterite in-situ U-Pb dating, are the common isotopic geochronological methods used in W deposits (Guo et al., 2016; Guo et al., 2018; Yuan et al., 2018; Yang et al., 2020). However, scheelite Sm-Nd dating should be carried out with caution (Li et al., 2021). The use of the Sm-Nd isotope system assumes that the fluid is homogeneous and the minerals have remained closed systems (Dickin, 2005; Li et al., 2021). Scheelite generally shows complex texture and multi-generation mineralization that will challenges the meaning of Sm-Nd scheelite ages. Other hydrothermal minerals generally show an ambiguous or even no genetic relationship with tungsten minerals that may provide inaccurate ages of W mineralization (Yang et al., 2020; Liu et al., 2022). By contrast, wolframite in-situ U-Pb LA-ICP-MS dating as an emerging geochronology protocol can produce a reliable W mineralization age. It has attracted rapidly growing attention from scholars that show its potential application (Deng et al., 2019; Tang et al., 2020; Yang et al., 2020).

The Yangxie ore district is located at the southern margin of the North Qinling Orogenic Belt, China. It consists of a large number of Au and W ore deposits/spots which makes it an important W-Au polymetallic metallogenic belt in the Qinling Orogenic Belt (Ge et al., 2020). The Yangwuchang and Dashegou deposits are two typical deposits in the Yangxie ore district that have been mined continuously for more than ten years. They are located at the intersection of two magmatic belts from the Late-Triassic and Jurassic-Cretaceous, both of which are directly associated with W-Au mineralization. Due to complicated magmatism, the mineralization ages and characteristics of the deposits are still controversial (Yu, 2017; Ge et al., 2020, 2021). To figure out the mechanism of W-Au mineralization, as well as the metallogenic characteristics of the W-Au deposit in the Qinling Orogenic Belt. In this paper, we reported cathodoluminescence (CL) and trace elements of scheelite combined with U-Pb dating of wolframite to constrain the timing of W mineralization, source, nature, and evolution of the ore-forming fluids, and the ore-forming processes.

2. Geological background

The Qinling Orogenic Belt is an important part of central China that connects the North China Block and South China Block (Fig. 1a). It is a composite continental orogenic belt with 1500 km long and 200–250 km wide. The Qinling Orogenic Belt formed as a result of longstanding subduction-collision orogenesis between the paleocontinent plates of the North China Block and South China Block (Zhang et al., 1995; Chen et al., 2000, 2006; Mao et al., 2011). It started in the middle Palaeozoic with the northward subduction of the Proto-Tethyan Ocean and the collision between the Qinling microplate and the North China Block along the Shang-Dan suture zone. It ended with the subduction of the Paleo-Tethyan Ocean and collision with the South China Block along the Mian-Lue suture zone in the early Mesozoic. The final collision is characterized by a scissor-like closure that propagated progressively from east to west as the South China Block clockwise rotation (Dong et al., 2011; Liu et al., 2015; Wu et al., 2019). From north to south, the Qinling Orogenic Belt is divided into the southern margin of the North China Block, the North Qinling Belt, the South Qinling Belt, and the northern margin of the South China Block by the Lingbao – Lushan – Wuyang fault, the Luonan-Luanchuan Fault, the Shang-Dan suture zone and the Mian-Lue suture zone, respectively (Fig. 1b; Zhang et al., 1995; Meng and Zhang, 1999). Faults are well developed in the Qinling Orogenic Belt and generally show similar E-W trending to regional tectonic structures. Voluminous granitoids are widespread in the Qinling Orogenic Belt, mainly including Palaeozoic gabbro and granite, Late-Triassic granitoids, and Late-Jurassic to Early-Cretaceous granitoids (Dong et al., 2011; Liu et al., 2015; Wu et al., 2019).

Attributed to intense structure deformations and magmatic activities, the Qinling Orogenic Belt has become a globally well-known metallogenic belt that accumulates abundant mineral resources such as Au, Ag, Mo, W, Cu, Pb, Zn, Hg, Sb, Ba, etc. (Chen et al., 2000). The Qinling Orogenic Belt also can be divided into the West and East Qinling Orogenic Belt by the Baoji-Chengdu Railway (Liu et al., 2015). The East Qinling is an important metallogenic belt for Au, Mo, W, Ag, and Pb-Zn deposits, and one of the most important Mo-W ore provinces in China (Mao et al., 2008; Fig. 1c). Most Mo-W deposits in the East Qinling are porphyry or porphyry-skarn type, which are temporally and spatially related with Late-Jurassic to Early-Cretaceous granitoids, such as the Jinduicheng Mo-W deposit and Sandaozhuang Mo-W deposit (Mao et al., 2011; Zhan et al., 2021). As well, the Zhen'an W (Mo) ore district is a newly reported ore district in South Qinling that hosts numerous W deposits (Fig. 1b). They are genetically associated with regional Late-Triassic granitoids, including the Dongyang skarn & quartz-vein type W deposit, Qipangou quartz-vein type W-Mo deposit and Hetaoping quartz-vein W (Be) deposits (Liu, 2013; Dai et al., 2019; Han et al., 2021; Lei et al., 2021). In addition, some W mineralization also occurred in the West Qinling (e.g. Zhaishang Au (W) deposit, Xuehuashan W deposit; Liu et al., 2015).

3. Deposits geology

The Yangxie ore district is located at the southern margin of the North Qinling Orogenic Belt (Fig. 2a). The Neoproterozoic Yangxie gneiss suite is the main ore-hosting rock, which is a metamorphic intrusion disintegrated from the Qinling Group. It is eyeball-shaped and/or striated biotite plagioclase gneiss, composed of plagioclase (~45–50 %), quartz (~35 %), and a minor amount of biotite and amphibole (Ge et al., 2021). Some Paleoproterozoic amphibolite facies of the Qinling Group metamorphic rocks are exposed in the north of the ore district. As well, there is also a small amount of lower Palaeozoic

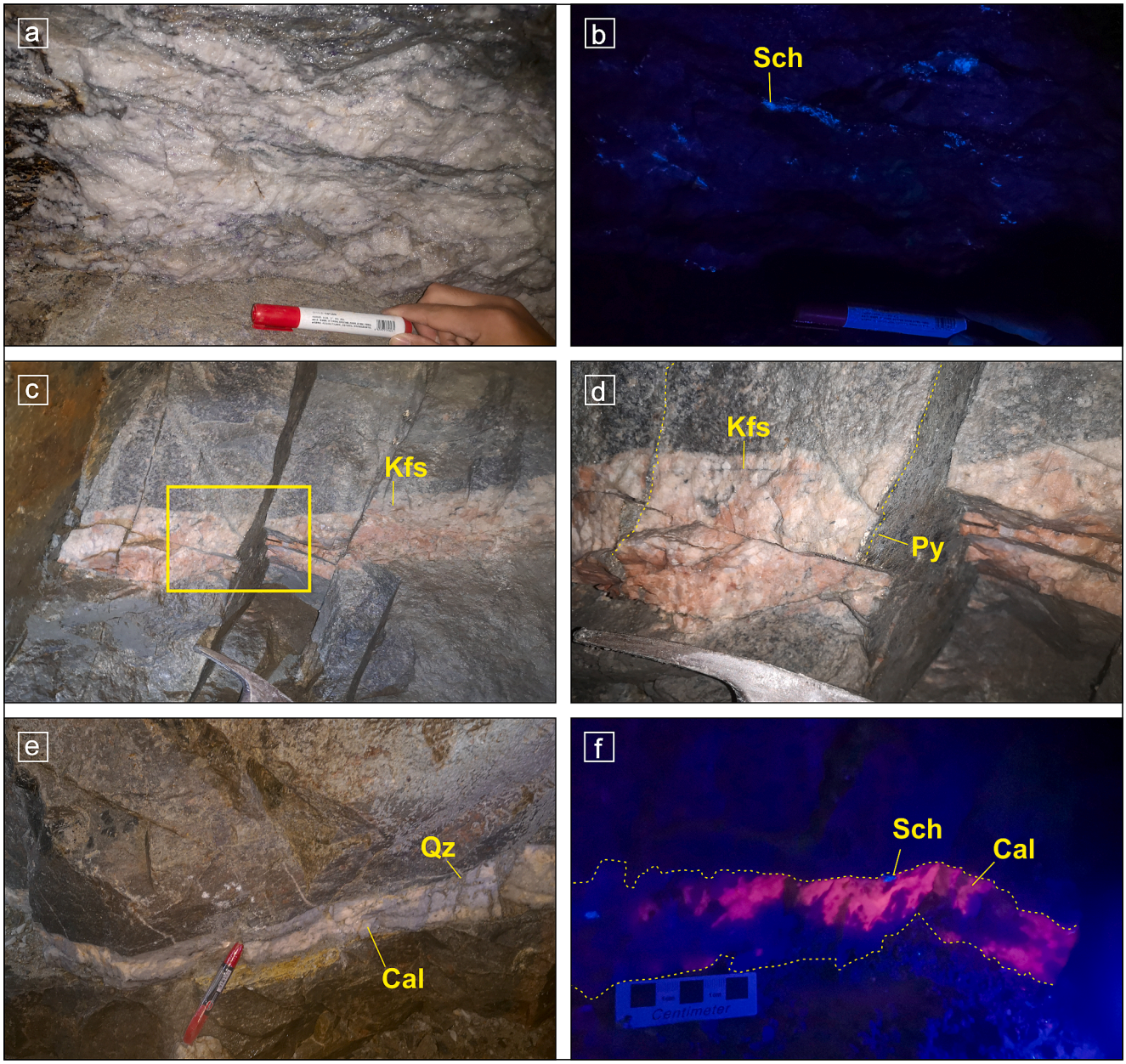

Fig. 3. Photographs of W mineralization characteristics in the Yangwuchang and Dashegou deposits. (a, b) scheelite veinlet host in quartz vein and under ultraviolet light. (c, d) Early mineralization stage K-feldspar vein in host rock crosscut by pyrite veinlets. (e, f) Late mineralization stage quartz-calcite vein with less scheelite and pyrite occur.

volcanic and clastic rocks and Devonian sedimentary rocks in the southern (Ge et al., 2020, 2021). Two periods of intrusions in the ore district are the Caledonian Qinwangshan mafic complex (422 ± 7 Ma; Ge et al., 2021) and the Indosinian granitoids of Caoping (221–215 Ma) and Shahewan (215–210 Ma; Hu et al., 2016). The W-Au mineralization in the ore district has a spatial relationship with the Shahewan granitoid. Fault structures are well developed in the Yangxie ore district, trending EW, NE, and NW. EW and NE trending faults and their subsidiary faults are the major structures controlling the distribution of the W-Au mineralization. Additionally, NW trending structures can also host independent Au-bearing quartz veins.

The Dashegou W deposit (Fig. 2b) has delineated at least 11 ore bodies, which could generally extend hundreds of meters but vary in thickness from 0.2 to 5.0 m with strikes NE-NEE and dip angles varying from 54° to 77° (Ge et al., 2021; Fig. 3a and b). Early quartz – K-feldspar veins are filled in the wall rock near the ore bodies and crosscut by pyrite veinlets (Fig. 3c and d). The late quartz-carbonate thin veins are <5 cm wide (Fig. 3e and f). The major ore minerals in the main mineralization stage are scheelite and wolframite, accompanied by tetrahedrite, sulfide, and hessite (Ag_2Te). The anhedral scheelite commonly encloses and crosscuts euhedral wolframite or occurs as veinlets in quartz fractures (Fig. 4). It also can coexist with tetrahedrite, pyrite, chalcopyrite as well as fluorite (Fig. 5). Very little scheelite can be found in the late quartz-calcite veins (Fig. 3e and f). Although limited gold was found in the Dashegou deposit, hessite occurs widely (Fig. 5d and e). Sulfide minerals are including pyrite, chalcopyrite, galena, and sphalerite. Quartz and fluorite are the main gangue minerals in this stage (Fig. 5a and b). Sericite is widely developed in the late quartz-calcite veins that enclose sulfides and scheelite. Wall rock alteration mainly consists of greisenization, potassic alteration, silicification, pyritization, fluoritization, and carbonation (Ge et al., 2020, 2021).

In the Yangwuchang W-Au deposit, at least 3 ore bodies have been

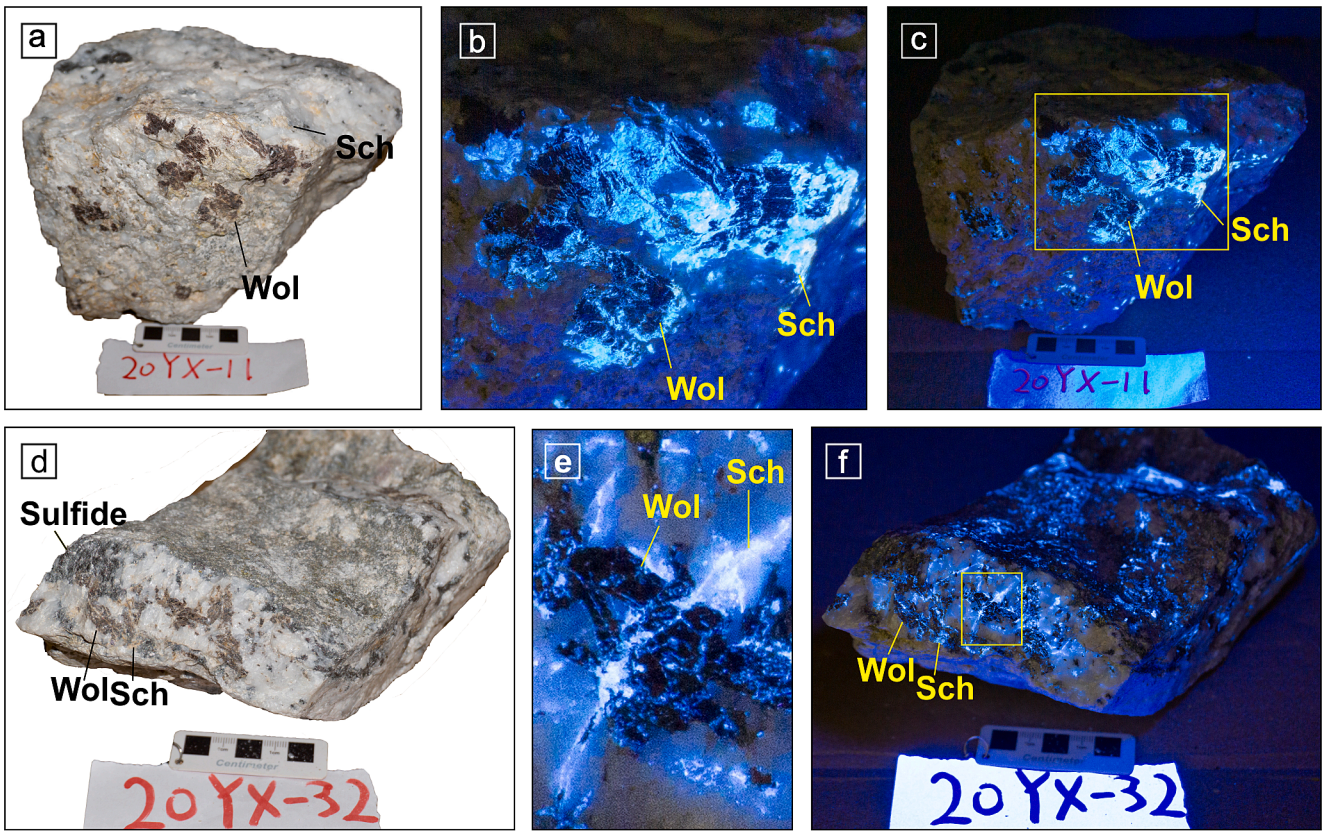

Fig. 4. Tungsten specimens in Yangwuchang (a, b) and Dashegou (c, d) deposits show scheelite crosscutting and closing wolframite. Mineral abbreviations: Cal-calcite; Kfs-K-feldspar; Py-pyrite; Qz-quartz; Sch-scheelite; Wol-wolframite.

delineated with a thickness of 0.3–3.33 m, strikes NE-NEE, and dip angles varying from 21° to 37°. Generally, it shows similar mineral assemblages compared with the Dashegou deposit, such as scheelite, wolframite, hessite, sulfides (tetrahedrite, pyrite, chalcopyrite, galena, and sphalerite), quartz, and fluorite (Figs. 6 and 7). In addition, bornite inclusion in pyrite (Fig. 6b) and scaly molybdenite in quartz veins (Fig. 6f) have been discriminated. Moreover, native gold occurred as fine-grained with a diameter range of 1 to 8 mm, which is closely associated with hessite (Fig. 7). The pyrite related to gold mineralization is characterized by well-developed fractures that crosscutting or enclose by veinlets of chalcopyrite and galena. Native gold, as well as hessite, is generally distributed in tetrahedrite or chalcopyrite veinlets.

According to mineral assemblages and crosscutting relationships, the mineralization process can be divided into four stages. The early mineralization stage is characterized by quartz + K-feldspar + pyrite assemblages. The main mineralization stage consists of wolframite + scheelite + native gold + hessite + tetrahedrite + pyrite + chalcopyrite + galena + sphalerite ± molybdenite ± bornite + fluorite. The late mineralization stage is composed of quartz + calcite + sericite + pyrite ± scheelite. The last stage is the supergene stage characterized by secondary minerals malachite, azurite and covellite. The mineral paragenesis in detail is illustrated in Fig. 8.

4. Sampling and analytical methods

4.1. Sampling

Scheelite and wolframite samples were collected from mining tunnels of the Yangwuchang and Dashegou deposits. Polished thin sections of selected samples were prepared for further analyses, including mineralogy, cathodoluminescence imaging, electron microprobe analysis (EMPA), and in-situ laser-ablation inductively-coupled plasma mass spectrometry (LA-ICP-MS) trace element analyses. Handpicked pure wolframite grains were mounted in epoxy and polished for the back-scattered electron (BSE) imaging and wolframite in-situ U-Pb dating analysis.

4.2. Electron microprobe analysis (EMPA)

Major element compositions of scheelite and wolframite were analyzed by a JEOL JXA 8230 electron probe microanalyzer equipped with four wavelength dispersive-type spectrometers at the Yanduzhongshi Geological Analysis Laboratories Co., ltd. The analysis was conducted with 15 Kv accelerating voltage, 10 nA beam current, and 5 um beam spot. The lower limits of detection of the measured elements vary between 0.01 and 0.05 wt%. ZAF procedure was used to correct data.

4.3. Cathodoluminescence (CL) and backscattered electron (BSE)

SEM-CL imaging of scheelite was performed using the FEI Nova NanoSEM450 equipped with Gatan MonoCL4 and OXFORD X-Max (50 mm^2) at the Key Laboratory of Deep-Earth Dynamics, Institute of Geology, Chinese Academy of Geological Sciences (CAGS). The analysis used an acceleration voltage of 7 kv and a working distance of 13.5 mm. Polished thin sections were carbon-coated before the analysis.

Carbon-coated epoxy mount of wolframite was photographed by a JSM-6700F field emission scanning electron microscope (FESEM) at Beijing GeoAnalysis Co., ltd.

4.4. Wolframite in-situ LA-ICP-MS U-Pb dating analysis

In-situ U-Pb dating of wolframite was analyzed by Agilent 7700x ICP-MS equipped with a GeoLasPro 193 nm ArF excimer laser at the

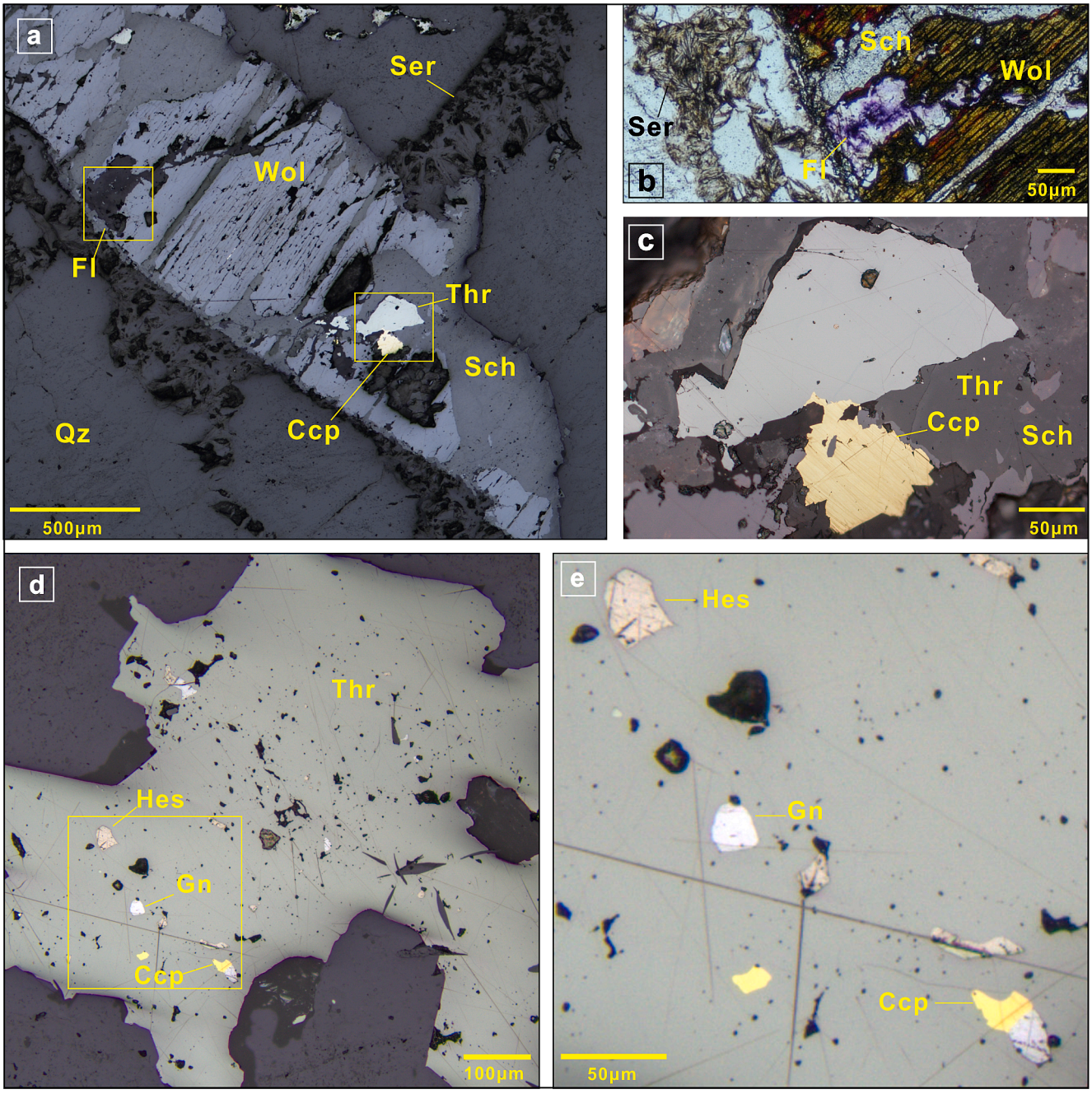

Fig. 5. Photomicrographs of mineral assemblage in the Dashegou W deposit. (a–c) sericite enclosed wolframite crosscut by scheelite, which coexists with tetrahedrite, chalcopyrite, and fluorite. (d–e) Hessite, galena, and pyrite coexist with tetrahedrite. Mineral abbreviations: Ccp-chalcopyrite; Gn-galena; Hes-hessite; Fl-fluorite; Py-pyrite; Sch-scheelite; Ser-sericite; Thr-tetrahedrite; Wol-wolframite.

State Key Laboratory of Ore Deposit Geochemistry, Institute of Geochemistry, Chinese Academy of Sciences (IGCAS), Guiyang, China. Before analysis started, a steady signal from NIST SRM610 glass was used to optimize mass response and minimize oxide levels to achieve maximum sensitivity while maintaining ThO/Th and U/Th ratios less than <0.3 % and ~1.0, respectively. NIST SRM 612, 614, and in-house wolframite standard MTM were used as the external isotopic calibration standards. The extracted samples were mixed with helium gas and then transported as an aerosol. Small amounts of nitrogen (3 mL/min) were added via a Y-junction to increase the sensitivity when the sample aerosol flowed out of the sample cell. Then, it was mixed with argon carrier gas via a *T*-connector (Hu et al., 2015) and flowed into the ICP-MS. 6 Hz laser repetition, 3 J/cm^2 energy density, and 32 μm spot size were used for this analysis. Each spot analysis consisted of a short laser pre-ablation (~8–10 pulses) for common Pb contamination elimination, a 20 s background acquisition, and a following 30 s sample data acquisition. Both analyses of NIST SRM 612 and in-house wolframite standard samples WT, WX, and YGX (Yang et al., 2020) were performed after every 15th tested-sample analysis. ICPMSDataCal (Liu et al., 2008) and Isoplot (Ludwig, 2003) were used to process raw data and calculate the U-Pb ages, respectively. The data error for isotopic ratios is 1 σ. Detailed operating conditions and processes are the same as the description by Tang et al (2020).

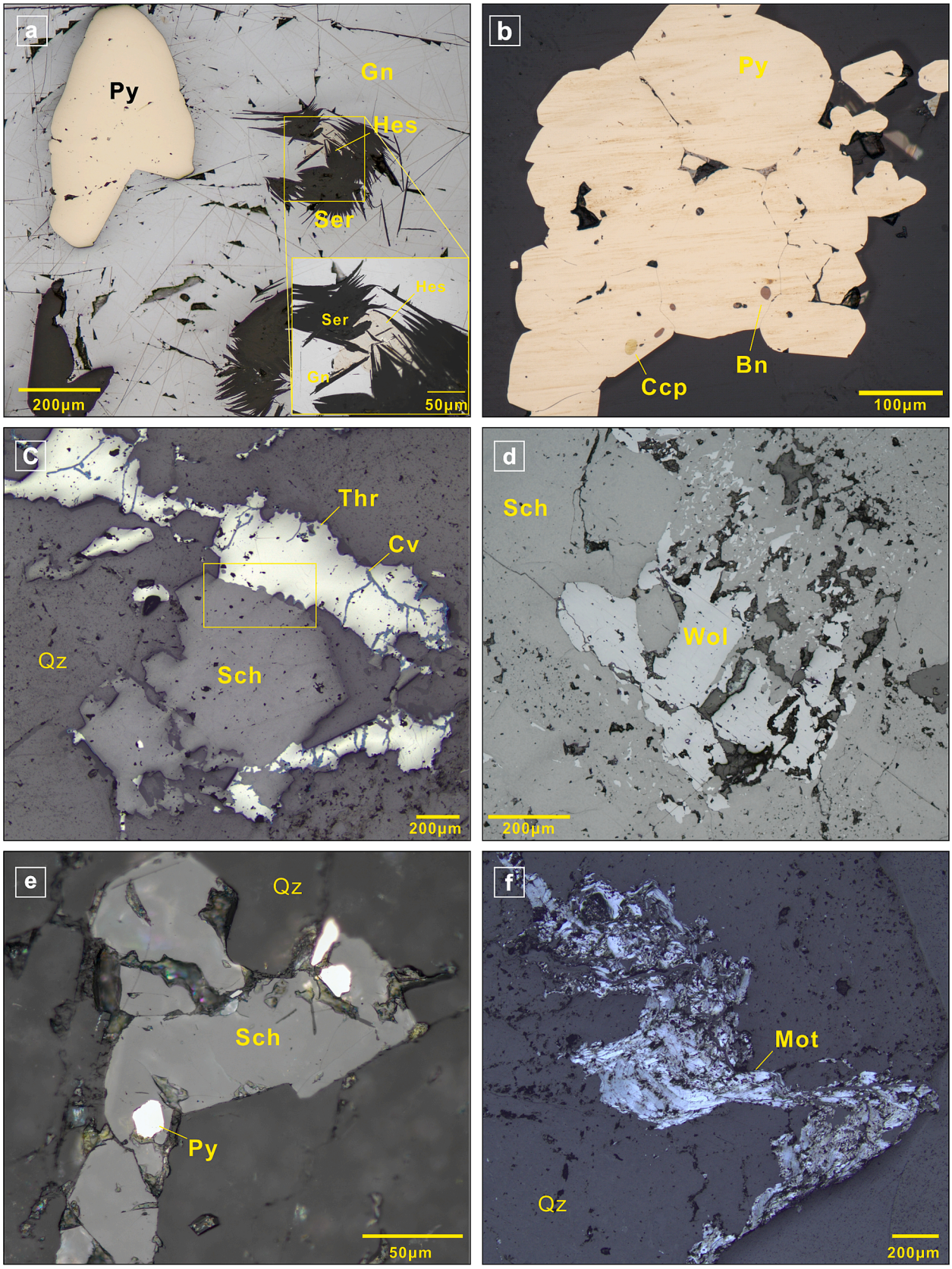

Fig. 6. Photomicrographs of mineral assemblage in the Yangwuchang W-Au deposit. (a) Hessite crosscut by sericite in galena. (c) Bornite and chalcopyrite inclusions in pyrite. (d) Tetrahedrite coexists with scheelite with small oxidized covellite. (e) Scheelite replacing wolframite. (f) Coexistence of scheelite and Pyrite. (g) Molybdenite in the W-bearing quartz veins. Mineral abbreviations: Bn-bornite; Ccp-chalcopyrite; Cv-covellite; Fl-fluorite; Gn-galena; Hes-hessite; Mot-Molybdenite; Py-pyrite; Qz-quartz; Sch-scheelite; Ser-sericite; Thr-tetrahedrite; Wol-wolframite.

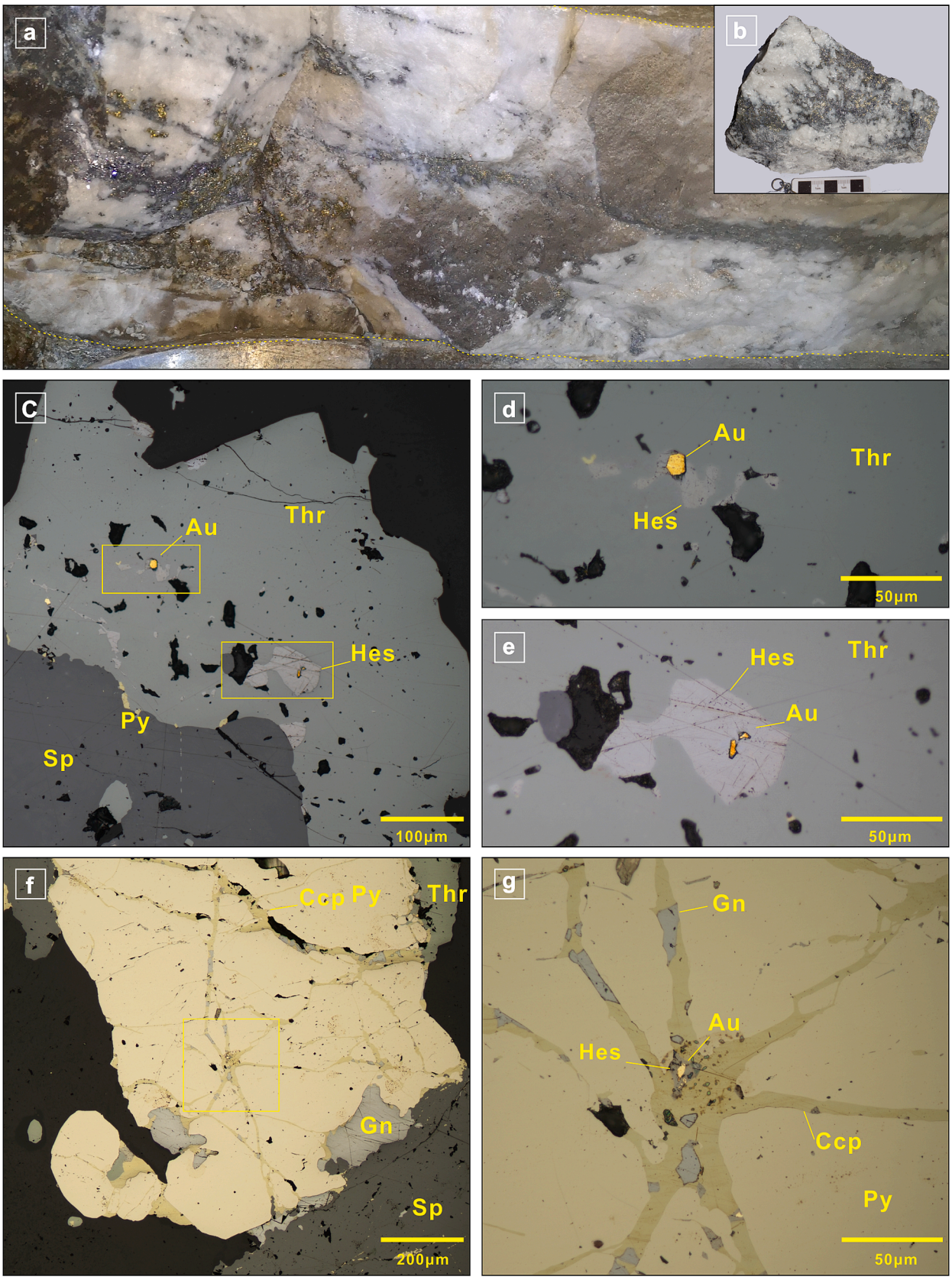

Fig. 7. Photographs and photomicrographs of quartz-vein type Au mineralization in the Yangwuchang W-Au deposit. (a–b) Au-bearing quartz-vein with numerous bedded sulfides. (c–e) native gold and hessite enclosed in tetrahedrite. (f–g) native gold and galena enclosed in chalcopyrite veinlet and crosscut by pyrite. Mineral abbreviations: Ccp-chalcopyrite; Gn-galena; Hes-hessite; Py-pyrite; Sp-sphalerite; Thr-tetrahedrite.

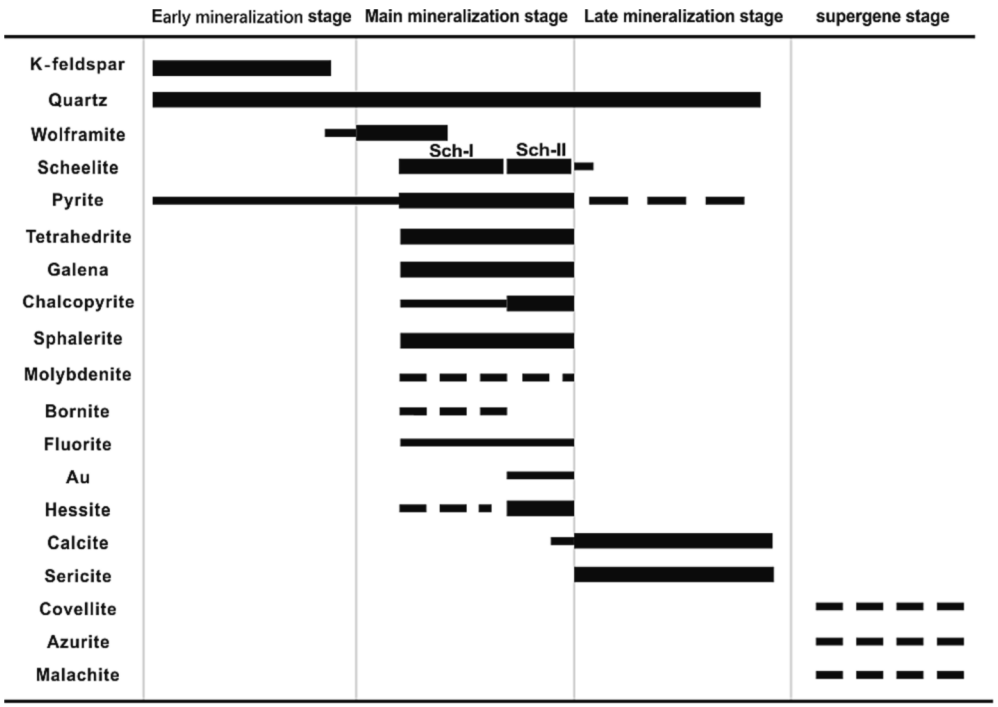

Fig. 8. Mineral paragenesis for the Yangwuchang and Dashegou deposits.

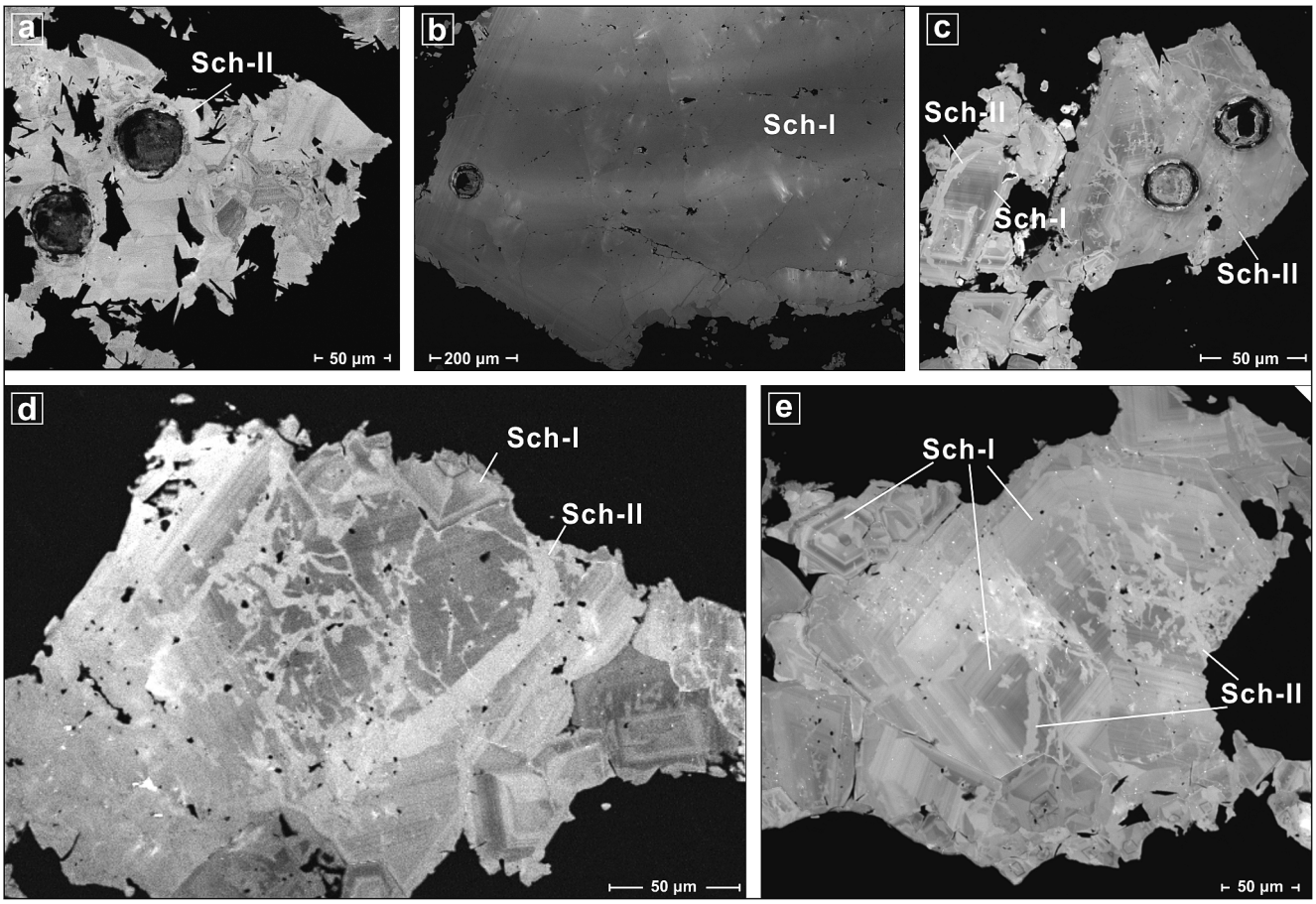

Fig. 9. Cathodoluminescence imagings of scheelite in the Yangwuchang (a, b) and Dashegou deposits (c–e). Sch-I: CL-dark gray, mostly present oscillating zones and crosscut by Sch-II. Sch-II: CL-bright gray, homogeneous imagings (b), overgrowth (c–d), and crosscutting Sch-I.

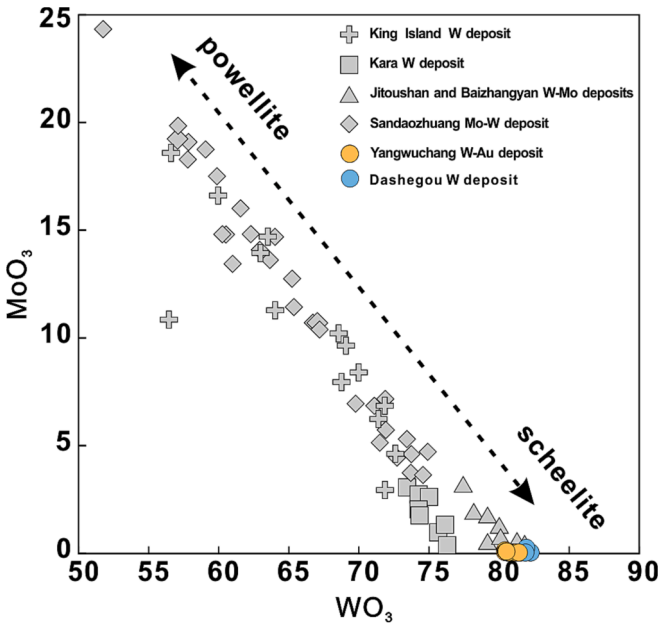

Fig. 10. Plots of MoO_3-WO_3 of scheelite. Scheelite data from other W deposits for comparison (Kwak and Tan, 1981; Zaw and Singoyi, 2000; Song et al., 2014; Sun and Chen, 2017; Zhan et al., 2021).

4.5. LA-ICP-MS trace element analysis

Trace elements composition of scheelite and wolframite were measured at the Wuhan Sample Solution Analytical Technology Co. ltd., Wuhan, China. Laser sampling was obtained using a GeoLasPro laser ablation system that consists of a COMPexPro 102ArF 193 nm excimer laser and a MicroLas optical system, then connected to an Agilent 7700e ICP-MS instrument. Helium and argon were used as the carrier gas and the make-up gas respectively and mixed by a *T*-connector before entering the ICP. A "wire" signal smoothing device is included in this laser ablation system (Hu et al., 2015). The spot size of the laser is 50 μm and the frequency is 10 Hz. Each spot analysis incorporated a 20 s background acquisition followed by a 50 s sample data acquisition. NIST SRM 610 was analyzed once after every tenth sample analysis to correct the time-dependent drift of sensitivity and mass discrimination. Reference glasses (BHVO-2G, BCR-2G, and BIR-1G) were analyzed at the beginning and the end of each analytical batch as external standards. The following masses were measured and the resulting average detection limits are reported in ppm (in parentheses): ^{7}Li (0.54), ^{9}Be (0.23), ^{11}B (4.30), ^{23}Na (0.01), ^{45}Sc (0.22), ^{51}V (0.54), ^{53}Cr (2.80), ^{55}Mn (<0.01), ^{59}Co (0.31), ^{60}Ni (2.36), ^{63}Cu (0.45), ^{66}Zn (0.87), ^{71}Ga (0.30), ^{75}As (2.11), ^{85}Rb (0.16), ^{88}Sr (0.04), ^{89}Y (0.01), ^{90}Zr (0.07), ^{93}Nb (0.01), ^{95}Mo (0.06), ^{107}Ag (0.05), ^{111}Cd (0.48), ^{118}Sn (0.95), ^{121}Sb (0.94), ^{125}Te (0.11), ^{133}Cs (0.06), ^{137}Ba (0.07), ^{139}La (0.01), ^{140}Ce (0.01), ^{141}Pr (<0.01), ^{146}Nd (0.03), ^{147}Sm (0.03), ^{151}Eu (0.01), ^{155}Gd (0.03), ^{159}Tb (<0.01), ^{163}Dy (0.02), ^{165}Ho (<0.01), ^{167}Er (0.01), ^{169}Tm (<0.01), ^{173}Yb (0.02), ^{175}Lu (<0.01), ^{178}Hf (0.01), ^{181}Ta (<0.01), ^{182}W (1.37), ^{205}Tl (0.02), ^{209}Bi (0.04), ^{208}Pb (0.03),^{232}Th (0.03), and ^{238}U (<0.01). All analytical data were processed using ICPMSDataCal software (Liu et al., 2008).

5. Results

5.1. Cathodoluminescence (CL) and backscattered electron (BSE) imaging

A total of 8 representative scheelite grains were examined from the main mineralization stage of the Yangwuchang and Dashegou deposits. At least three generations of scheelite can be clearly discriminated by the different CL responses and texture features in CL imaging (Fig. 9), as well as the different mineral paragenesis. Sch-I grains are characterized by weak responses and oscillatory zonation patterns in CL imaging. By contrast, Sch-II grains have strong intensity and homogeneous patterns that enclose and crosscut Sch-I. In addition, it should classify scheelite in the late mineralization stage as Sch-III (Fig. 3f). However, it is not mentioned in this study due to difficult sampling.

Wolframite displays large-sized (5–20 mm) euhedral crystals in hand specimens. Most grains still preserve partial sharp boundaries after crushing and separating (1–2 mm). All wolframite grains show homogeneous BSE imaging without any oscillatory zones.

5.2. Major elements

The EMPA results of scheelite and wolframite are summarized in ESM Tables 1, 2. Both scheelite and wolframite in the Yangwuchang and Dashegou deposits exhibit stable major element compositions. Scheelite grains have an average chemical formula of $Ca_{0.95}W_{1.01}O_4$ including 18.16–18.65 wt% CaO and 80.42–82.24 wt% WO_3, the sum of which has up to 99 wt%. Compared with the scheelite from other W deposits, our samples have a consistent content with much lower MoO_3 concentrations (Fig. 10).

Wolframite samples are composed of 0.08–2.42 wt% FeO, 22.15–24.62 wt% MnO and 54.22–65.44 % WO_3. The average chemical formula is $(Mn_{1.02}Fe_{0.03})_{\Sigma 1.05}W_{0.98}O_4$ that Fe/(Fe + Mn) ratios of 0.00–0.10 are closer to the hübnerite end-member ($MnWO_4$).

5.3. Trace elements of scheelite and wolframite

A total of 48 scheelite and 30 wolframite trace element analyses were performed by the in-situ LA-ICP-MS method (ESM Table 3, 4). The chondrite-normalized REE patterns are shown in Fig. 11.

Sch-I has variable abundances of Na (1.51–73.92 ppm, avg. 30.41 ppm), Sr (718.77–1667.91 ppm, avg. 1258.97 ppm), Mn (6.05–458.78 ppm, avg. 46.50 ppm), Y (10.76–837.44 ppm, avg. 165.68 ppm), Nb (0.65–24.56 ppm, avg. 4.62 ppm), Mo (7.47–189.99 ppm, avg. 62.25 ppm) and U (0.32–29.27 ppm, avg. 5.60 ppm). Compared with Sch-I, Sch-II is relatively enriched in Na (2.64–117.73 ppm, avg. 39.50 ppm), Mn (0.99–3386.00 ppm, avg. 304.78 ppm), Y (54.21–821.54 ppm, avg. 285.09 ppm), Nb (1.39–24.90 ppm, avg. 9.85 ppm) and Mo (4.41–767.92 ppm, avg. 328.29 ppm), and depleted in Sr (481.23–1310.86 ppm, avg. 919.50 ppm) and U (0.02–13.10 ppm, avg. 2.03 ppm; Fig. 12). The concentrations of other trace elements are close or below the detection limit. The total rare earth element (ΣREE + Y) concentrations of Sch-I and Sch-II range from 51.78 to 2143.29 ppm (avg. 583.74 ppm) and 171.90–2434.30 ppm (avg. 1005.58 ppm), respectively. Two distinct types of chondrite-normalized REE patterns can be distinguished (Sun and McDonough, 1989; Fig. 11e). Sch-I is characterized by MREE depleted and sightly right-inclined (La_N/Yb_N = 0.48–3.33, avg. 1.56) patterns with strong positive Eu anomalies (Eu/Eu* = 0.96–28.42, avg. 5.37). Sch-II is MREE enriched and sightly left-inclined (La_N/Yb_N = 0.31–3.46, avg. 0.85) REE patterns with slightly positive Eu anomalies (1.20–1.46, avg. 1.53).

The trace element concentrations of wolframite show a narrow range, notably Sc (7.16–54.20 ppm, avg. 27.58 ppm), Zn (4.34–42.8 ppm, avg. 13.90 ppm), Zr (15.90–47.44 ppm, avg. 23.18 ppm), Nb (14.97–119.57 ppm, avg. 50.83 ppm), U (0.27–16.79 ppm, avg. 6.83 ppm). Excluding two outliers (582.34 and 103.54 ppm), the content of Cr ranges from 0.11 to 47.75 ppm with an average of 15.00 ppm. Other trace element concentrations are close to or below the detection limit. The contents of ΣREE + Y range from 3.56 to 141.11 ppm and mainly > 10 ppm. The wolframite has a uniform chondrite-normalized REE pattern with strongly LREE depleted (Fig. 11c, d, and f; La-Nd = 0.01–0.96 ppm, avg. 0.17 ppm), moderate MREE (Sm-Ho = 0.48–27.09 ppm, avg. 11.20 ppm), HREE enriched (Eu-Lu (+Y) = 3.03–113.80 ppm, avg. 41.35 ppm) and obvious left-inclined REE pattern (La_N/Yb_N =

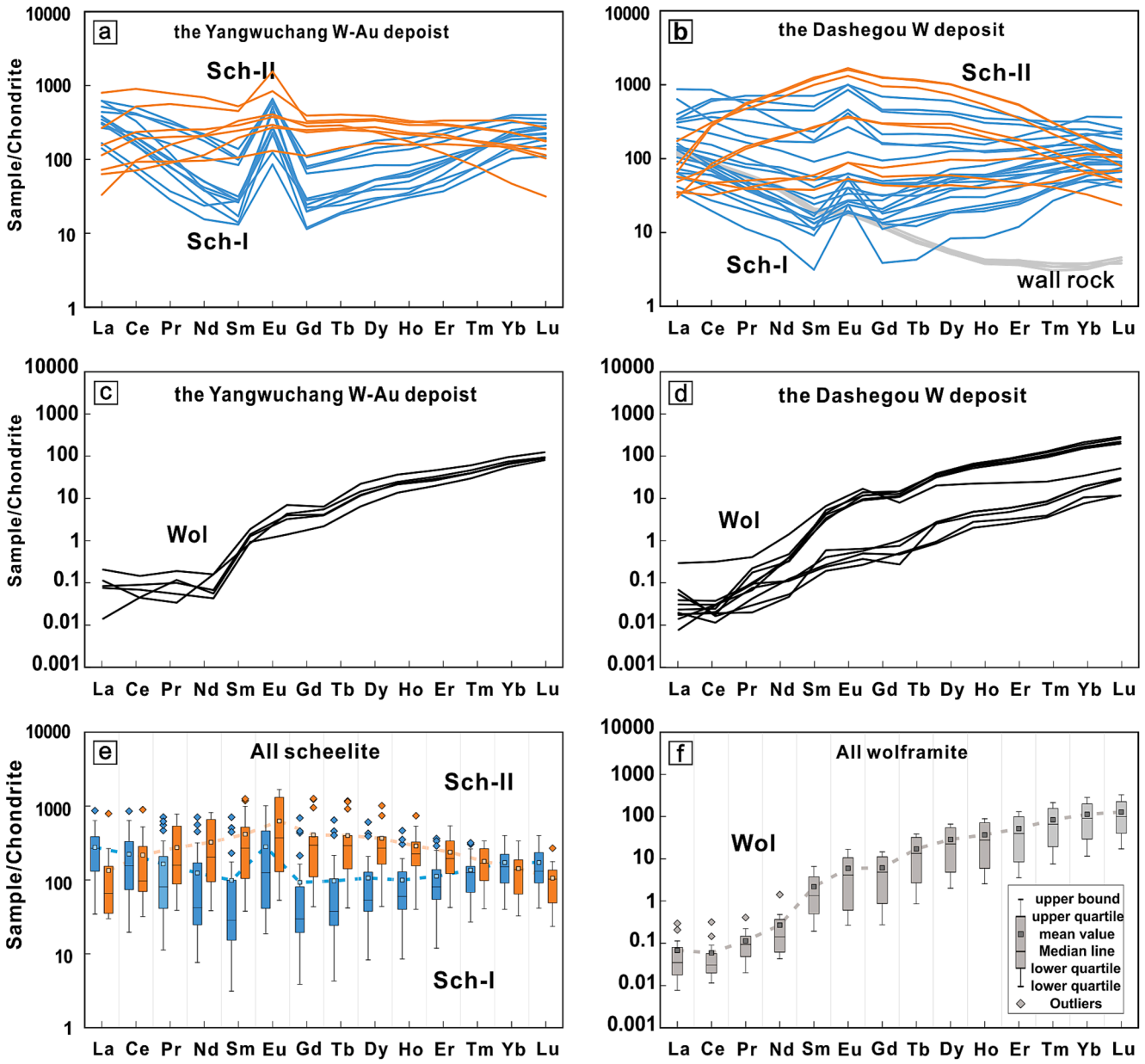

Fig. 11. Chondrite-normalized REE patterns of scheelite and wolframite in the Yangwuchang and Dashegou deposits. (a, b) Sch-I is characterized by strong positive Eu anomaly and MREE-depleted REE patterns, and Sch-II is bell-shaped MREE-enriched and slightly Eu anomaly. (c, d) Wolframite shows negligible Eu anomaly and left-inclined REE patterns. (e, f) box diagrams of two-generation scheelite and wolframite. (b). Wall rock of the Yangxie ore district is collected from Ge et al. (2021). The normalization values were from Sun and McDonough (1989).

0.00–0.009, avg. 0.002).

5.4. U-Pb dating of wolframite

The results of wolframite in-situ U-Pb isotope analysis are presented in ESM Table 5, and U-Pb Tera-Wasserburg diagrams are plotted in Fig. 13.

The wolframite sample YX37 from the Yangwuchang deposit has total Pb, Th, and U concentrations of 0.09–0.78, 0.00–0.07, and 0.61–31.53 ppm, respectively, and yields a lower intercept $^{206}Pb/^{238}U$ age of 139.1 ± 2.0 Ma (1 σ, n = 13, MSWD = 1.4; Fig. 13a).

The wolframite sample YX24 from the Dashegou deposit has total Pb, Th, and U concentrations ranging from 0.30 to 3.10, 0.00 to 0.51, and 1.94 to 77.87 ppm respectively, and obtains a lower intercept $^{206}Pb/^{238}U$ age of 141.5 ± 4.5 Ma (1 σ, n = 33, MSWD = 3.8; Fig. 13b).

The wolframite sample YX32 from the Dashegou deposit has low Pb (0.13–0.90 ppm), low Th (0.00–0.32 ppm), varying U (0.62–30.67 ppm) and yields a lower intercept $^{206}Pb/^{238}U$ age of 141.8 ± 6.4 Ma (1 σ, n = 20, MSWD = 1.8; Fig. 13c).

6. Discussion

6.1. Timing of W-Au mineralization

Most W deposits are temporally and genetically related to highly evolved granitic stocks (Korges et al., 2018; Yuan et al., 2019). The Yangwuchang and Dashegou deposits have a close spatial relationship with the Late-Triassic Shahewan granitoid (221–210 Ma; Hu et al., 2016). As well, a small amount of W-Au geochemical anomalies occurred around or inside the granitoid. In addition, the genetic relationship between the Zhen'an W-Mo ore district and the Late-Triassic granitoid in the southwest of the Yangxie ore district, such as the

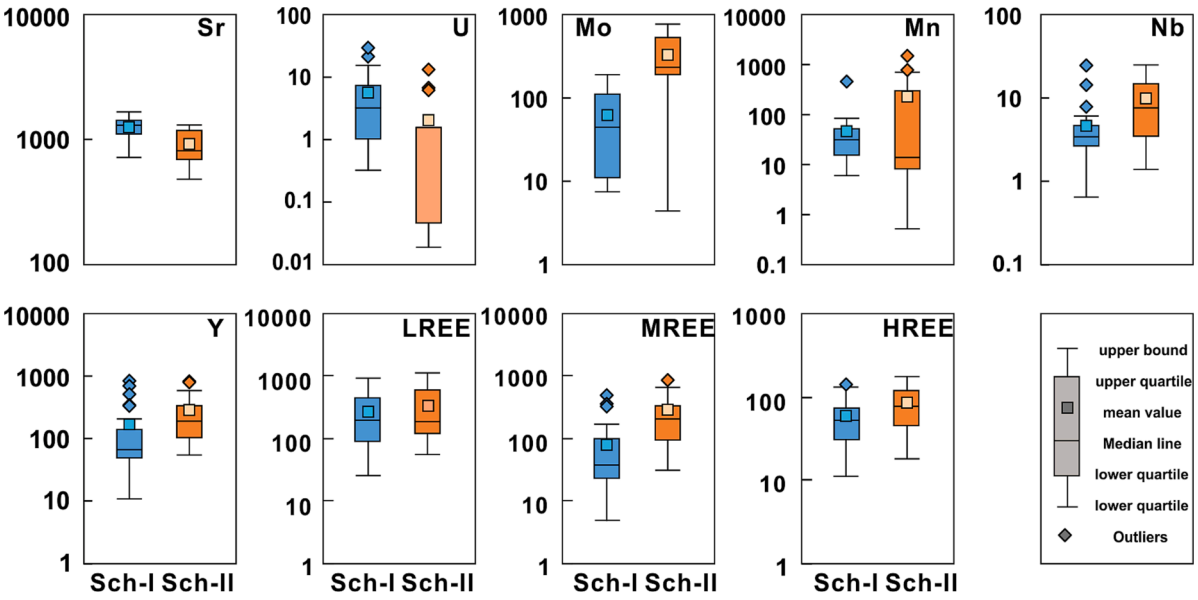

Fig. 12. Box plots of trace elements contents (ppm) of Sch-I and Sch-II.

Qipangou W-Mo deposit (199.7 ± 3.9 Ma; Han et al., 2021) and the Lanbandeng monzogranite (222.7 ± 2.3 Ma; Han et al., 2021), also implies the important role of the Late-Triassic magmatism in the W mineralization in the Qinling Orogenic Belt (Han et al., 2021). Based on these, previous studies deduced that the W-Au mineralization in the Yangwuchang and Dashegou deposits may be genetically related to the Late-Triassic mechanism (Ge et al., 2020, 2021).

Wolframite in-situ U-Pb dating by LA-ICP-MS can constrain the W metallogenic age directly and accurately. In this study, homogeneous BSE images and stable trace element compositions of wolframite indicate that it formed in one generation and with no intense post-transformation subjection (Fig. 11c, d, and 13). Our in-situ U-Pb dating of wolframite provided ages of 141.8–139.1 Ma for the W mineralization. The considerably younger ore-forming ages than the Shahewan granitoid indicate that the W mineralization in this area is temporally and genetically unrelated to Late-Triassic magmatism. Therefore, any exploration based on a mineralization model involving a genetic link with Late-Triassic magmatism would be inappropriate. Moreover, the W mineralization ages perfectly match the age of Au mineralization in this ore district analyzed by Au-bearing pyrite Re-Os dating (141 ± 18 Ma; Yu, 2017). The W-Au ages are within the range of the Late-Mesozoic Mo-W-Au-Pb-Zn polymetallic metallogenic belt in the East Qinling Orogenic Belt (Fig. 13d). The deep magma/mantle material source and geodynamic setting of lithospheric thinning and extension account for magmatism and metallogenesis (Mao et al., 2005, 2008,2011; Yu, 2017; Zhao et al., 2018). Hence, we suggest that the W-Au mineralization in the Yangwuchang and Dashegou deposits should be associated with Early-Cretaceous magmatism.

6.2. Correlation between cathodoluminescence intensity and elemental composition

Cathodoluminescence (CL) is a technique capable of identifying complicated inner textures, zonation patterns, and trace element distributions of minerals. Generally, the intensity of CL can be affected by intrinsic and extrinsic defects. Intrinsic defects refer to site vacancies, structural imperfections (e.g. poor ordering, radiation damage, and shock damage), and impurities (non-activators that distort the lattice; Götze, 2002; Poulin et al., 2016). For scheelite, the self-luminescence band (SB) is the most important intrinsic factor contributed by the WO_4^{2-} group (Grasser et al., 1988; Brugger et al.,2000a). The extrinsic contribution is mainly caused by trace elements in scheelite structures which can be subdivided into activators, quenchers, and neutral elements. Activators can promote CL responses by releasing the absorbed energy as photons, represented by transition metals such as Mn, Nb, and REEs. On the contrary, quenchers can inhibit or eliminate CL responses by trapping absorbed energy, like Mo, U, Co, and Ni (Götze, 2002; MacRae et al., 2009; Rusk, 2012; Poulin et al., 2016; Su et al., 2019). Neutral elements are those which do not affect the luminescence response (e.g. Sr and As; Poulin et al., 2016). Thus, the CL intensity of scheelite is a complex balance between each of these factors (Brugger et al.,2000a; Götze, 2002; MacRae et al., 2009; Rusk, 2012; Poulin et al., 2016; Su et al., 2019).

Excluding trace elements with low content (<0.1–1 ppm) which play a negligible role in CL intensity, the trace elements most likely to affect CL intensity are Sr, U, Mo, Mn, Nb, Y, and REEs (Fig. 12). Strontium content is high enough and displays a noticeable change between two generations of scheelite. However, Sr is a neutral element whose content changes will not affect the CL intensity (Poulin et al., 2016; Li et al., 2021). Uranium can inhibit the CL response of scheelite. It can decrease the intensity of the self-luminescence band by substituting W^{6+} (mechanism V) and destroying structures of scheelite by self-irradiation (Lenz and Nasdala, 2015; Su et al., 2019). Nevertheless, considering the relatively low content of U (<1–10 ppm), the effect of U is considered to be negligible. Previous studies suggest that molybdenum content, as a quencher, should be negatively related to CL intensity (Brugger et al.,2000a). However, in this study, Sch-II with higher Mo content has a more intense CL response than Sch-I. This implies that other stronger activators should exist to compensate for the effects of Mo and U. Therefore, the CL intensity of scheelite should be mainly controlled by activator elements of REEs, Y, Mn, and Nb whose contents positively correlate with CL intensity. Compared with MREE, Y, and Mn, the contents of LREEs, HREEs, and Nb show a slight change between Sch-I and Sch-II which may contribute less to CL intensity. Hence, the different CL intensities between Sch-I and Sch-II are mainly controlled by the elements of MREEs, Y and Mn (Fig. 12g).

6.3. Substitution mechanisms of trace elements into scheelite

Trivalent REEs can incorporate into scheelite through substitution with divalent Ca. Meanwhile, a charge compensation mechanism is necessary to maintain charge balance and crystal structure stability

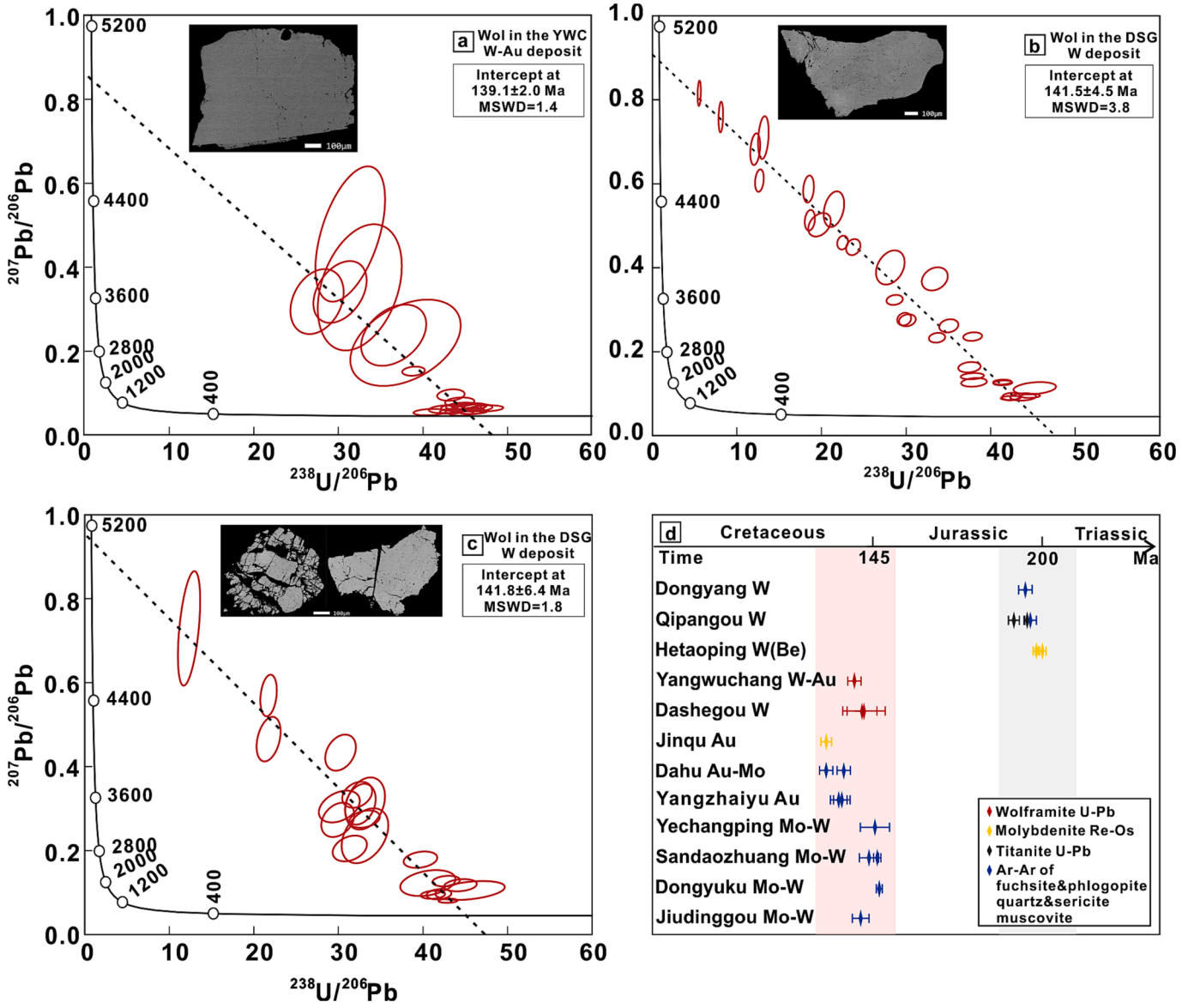

Fig. 13. (a–c) Tera-Wasserburg plots and the lower intercepts ages of wolframite samples from the Yangwuchang and Dashegou deposits. (d) Summary diagram of W and Au metallogenic ages in the East Qinling Orogenic Belt (Mao et al., 2008; Zhu et al., 2010; Li et al., 2012; Zhang, 2014; Zhang et al., 2015; Zhou et al., 2020; Lei et al., 2021).

(Nassau and Loiacono, 1963; Burt, 1989; Ghaderi et al., 1999). The most well-recognized and widely proven substitution mechanisms are as follows:

$2Ca^{2+}=(REE + Y)^{3+}+Na^{+}$(I)

$Ca^{2+}+W^{6+}=(REE + Y)^{3+}+(Nb,Ta,V)^{5+}$(II)

$3Ca^{2+} = (2REE)^{3+} + \square Ca$ (site vacancy)(III)

Divalent valence ions such as Eu^{2+}, Sr^{2+}, Fe^{2+}, Pb^{2+}, and Mn^{2+} can also substitute under mechanism IV. Mo^{6+} can substitute with W^{6+} and form scheelite-powellite ($CaMoO_4$) solid solution. U^{6+} and As^{5+} also can substitute into scheelite under mechanism V (Poulin et al., 2018; Su et al., 2019).

$Ca^{2+}\leftrightarrow Eu^{2+}$, Sr^{2+}, Fe^{2+}, Pb^{2+}, Mn^{2+}(IV)

$W^{6+}\leftrightarrow Mo^{6+}$, U^{6+}, As^{5+}(V)

In mechanism I (or II), each substitution of $(REEs + Y)^{3+}$ requires a Na^{+} or $(Nb, Ta, V)^{5+}$ to balance charges, which means the scheelite should display a positive correlation between the contents of ΣREE + Y and Na (or Nb + Ta + V). The degree of substitution under mechanisms I or II is depend on the contents of Na and Nb + Ta + V in scheelite. Moreover, $(REEs + Y)^{3+}$ will substitute into scheelite with Ca^{2+} preferentially, whose radius is close to the average size of REE^{3+} instead of Ca^{2+} ($_{r}REE^{3+}$ = 1.06 Å, $_{r}Eu^{3+}$ = 1.066 Å, $_{r}Ca^{2+}$ = 1.12 Å; Shannon, 1976; Ghaderi et al., 1999). Hence, scheelite will display an MREE-enriched REE pattern when mechanism I is the main mechanism (Ghaderi et al., 1999; Brugger et al., 2000b). In contrast, the site vacancy of mechanism III can reduce the rigidity of the Ca^{2+} site and remove the limitation of the $(REEs + Y)^{3+}$ radius, so each $(REEs + Y)^{3+}$ is independent and flexible without fractionation (Ghaderi et al., 1999). Thus, $(REEs + Y)^{3+}$ into scheelite by mechanism III can inherit the characteristics of the original ore-forming fluids (Song et al., 2014; Sun and Chen, 2017). Hence, we can identify the substitution mechanism of REEs by comparing the contents of ΣREE + Y-Eu (to exclude the impact of Eu^{2+}) with Na (or Nb + Ta + V). Positive correlations and close contents between Na (or Nb + Ta + V) and ΣREE + Y-Eu in scheelite suggest that mechanism I (or II) is the main substitution mechanism. Otherwise,

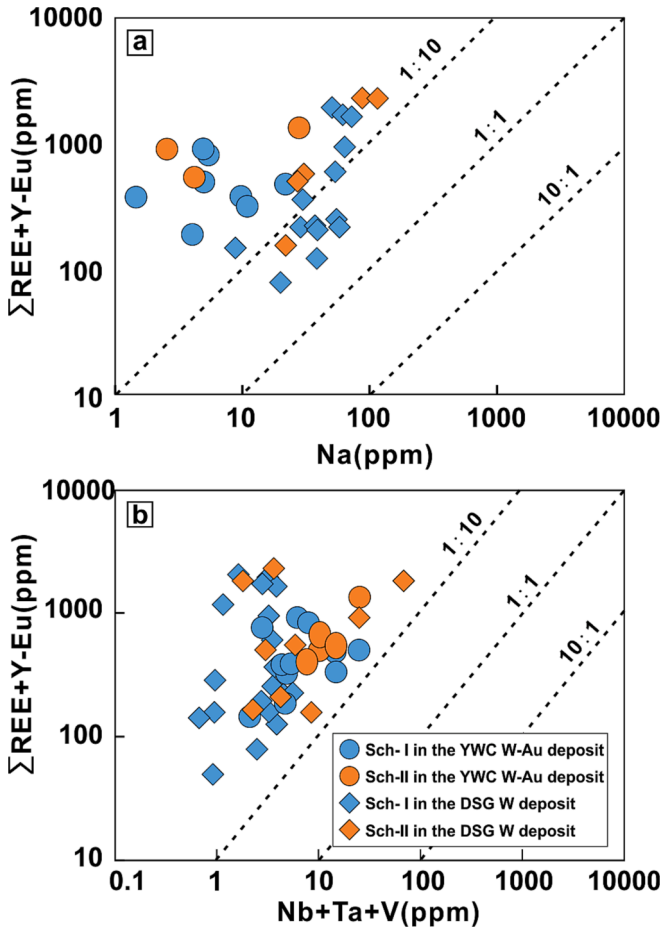

Fig. 14. (a) Scheelite plots of ΣREE + Y-Eu (ppm) *vs* Na (ppm). (b) Scheelite plots of ΣREE + Y-Eu (ppm) *vs* Nb + Ta + V (ppm). Dash lines represent ΣREE + Y-Eu (ppm)/ Na (ppm) or Nb + Ta + V (ppm) = 10, 1, 0.1, respectively.

mechanism III should be the major one.

In this study, both Na and Nb + Ta + V of scheelite are characterized by a lower content than that of ΣREE + Y-Eu, and most ratios of Na (or Nb + Ta + V)/ ΣREE + Y-Eu are <1:10 (Fig. 14). Furthermore, there are no obvious positive correlations either. Thus, it is clear that neither mechanism I nor II plays a significant role in the substitution of (REEs + Y)$^{3+}$, because the deficient contents of Na and Nb + Ta + V are hard to sustain the reactions in the ore-forming fluids. Mechanism III is the principal substitution mechanism of (REEs + Y)$^{3+}$ into scheelite so that the scheelite could inherit the REE characteristics of the ore-forming fluid.

6.4. Characteristic of Eu anomalies in scheelite

All scheelite from the Yangwuchang and Dashegou deposits show positive Eu anomalies, where Sch-I has obvious strong positive Eu anomalies, especially in the Yangwuchang deposit (average Eu/Eu* = 11.03), and Sch-II shows weak positive Eu anomalies (Fig. 11). The associated minerals particularly enriched in REEs will affect the contents of REEs in the ore-forming fluids and therefore influence the Eu anomaly of the scheelite. For instance, scheelite in skarn-type deposits is easily influenced by early crystalized REE-rich minerals like garnet (Song et al., 2014; Sun et al., 2019; Yuan et al., 2019). In this study, we analyzed the trace elements of wolframite which is the main paragenetic mineral of scheelite (Fig. 4a and d). However, the low and invariant REE contents of wolframite at both the Yangwuchang and Dashegou deposits suggest that it has a negligible and equal effect on REEs in scheelite (Fig. 11c and d). Thus, the associated minerals are not the reason for the

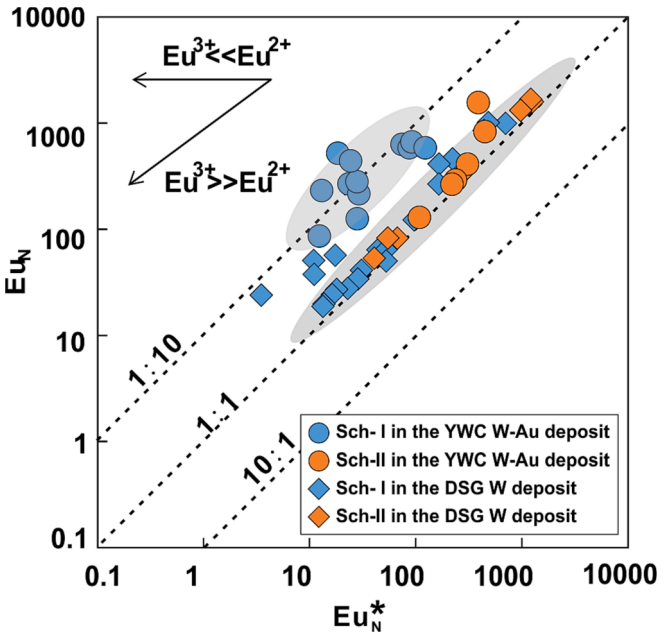

Fig. 15. Calculated Eu_N^* values *vs* chondrite-normalized Eu concentrations (Eu_N) where $Eu_N^* = (Sm_N{*}Gd_N)^{1/2}$.

variation of Eu anomalies of scheelite in the chondrite-normalized REE patterns.

Eu^{2+} is generally considered to be able to access the Ca^{2+} site in scheelite preferentially than $REEs^{3+}$ in a hydrothermal solution. Intense positive Eu anomalies appear when Eu^{2+} dominates ($Eu^{2+} \gg Eu^{3+}$), while no obvious effects or negative anomalies happen when Eu^{3+} dominates (Ghaderi et al., 1999; Brugger et al., 2000b). The valence state of Eu can be identified by analyzing the correlation between Eu, Sm, and Gd, which can be presented clearly by Eu_N *vs* Eu_N^* plot diagram [$Eu_N^* = (Sm_N{*}Gd_N)^{1/2}$; Ghaderi et al., 1999]. Eu^{3+} will be the main state when Eu_N has a positive linear correlation close to the 1:1 line with Eu_N^*, otherwise, it will be dominated by Eu^{2+}. As shown in Fig. 15, Sch-I from the Yangwuchang deposit is far from the 1:1 dashed line, which indicates that divalent Eu is dominant in the ore-forming fluids. The dominance of Eu^{2+} could perfectly explain the strong positive Eu anomaly of Sch-I in the Yangwuchang deposit, which should be released during plagioclase decomposition. By contrast, other scheelite displays an obvious positive correlation between Eu_N and Eu_N^* with a regular distribution along the 1:1 dashed line, indicating that Eu has a trivalent valence.

Europium is a redox-sensitive element, so Eu anomaly can be affected by the variation of redox conditions (Poulin et al., 2018) or inherited from the parent ore-forming fluids (Sun and Chen, 2017). Eu can exist as Eu^{3+} in an oxidizing environment and as Eu^{2+} in a reducing condition. In addition, molybdenum is a redox-sensitive element as well (Poulin et al., 2018; Han et al., 2020). In an oxidizing environment, Mo^{6+} can enter into scheelite by substituting W^{6+} and form scheelite-powellite ($CaMoO_4$) solid solution. By contrast, it precipitates as a tetravalent state to form molybdenite [MoS_2] in reducing conditions (Linnen and Williams-Jones, 1990; Rempel et al., 2009). As shown in Fig. 10, our samples have much lower MoO_3 concentrations than other W deposits precipitated under oxidizing environments, suggesting a strongly reducing environment. Though the increase of Mo content (Fig. 17a) may indicate the changing of redox condition, the slight change has negligible influence on the strongly reducing environment. Hence, redox changing of the ore-forming fluids is not the main cause of variation Eu anomalies. The Eu anomalies of scheelite are probably driven by parent ore-forming fluids and could record characteristics of

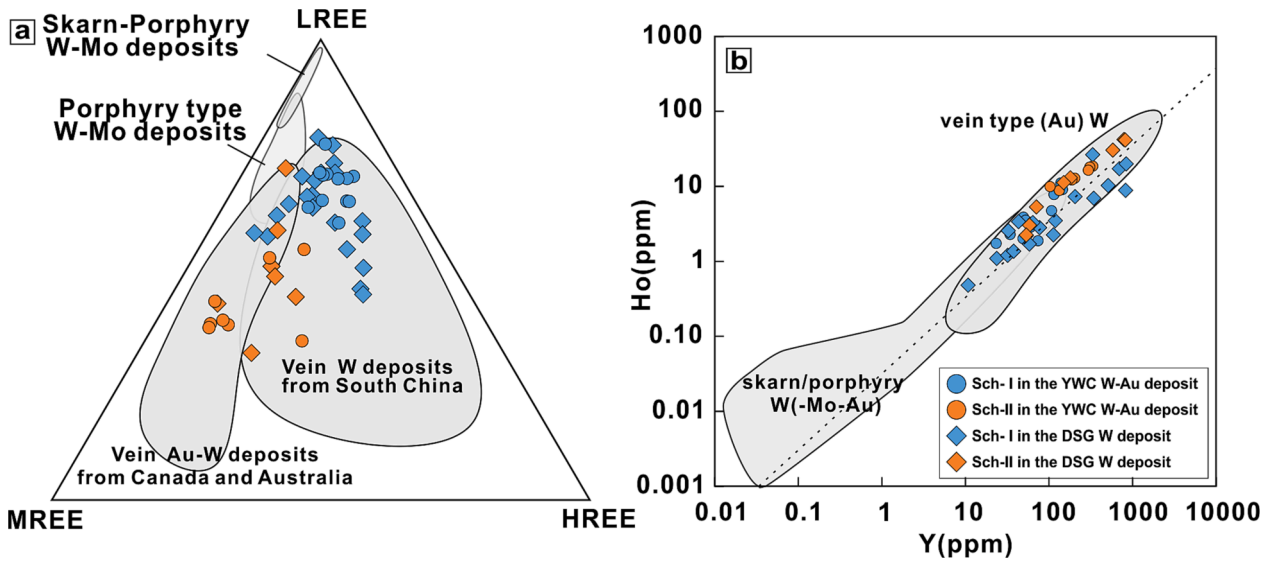

Fig. 16. (a) The LREE-MREE-HREE ternary diagram of scheelite. (b) scheelite plots of Y (ppm) *vs* Ho (ppm). The REEs data of scheelite was taken from (Dostal et al., 2009; Song et al., 2014; Wang et al., 2017; Liu et al., 2019; Song et al., 2019; Pan et al., 2020; Qin et al., 2020; Sciuba et al., 2020; Li et al., 2021; Zhan et al., 2021).

ore-forming fluids.

6.5. Source of the ore-forming fluids

Gold mineralization has similar assemblage minerals with scheelite such as tetrahedrite, pyrite, chalcopyrite, galena, and hessite (Figs. 5, 6a, and 10) that infer the close relationship between them. The similar mineralization ages of W (141.8–139.1 Ma) and Au (141 ± 18 Ma; Yu, 2017) in the Yangxie ore district also imply their close genetic relationship. Song et al. (2014) suggested the LREE-MREE-HREE ternary diagram of scheelite could use to distinguish different types of deposits and has been widely used by following scholars (Fu et al., 2017; Li et al., 2019; Yuan et al., 2019; Liu et al., 2021b). As shown in Fig. 16a, Sch-I is distributed in the range of vein-type W deposits near the corner of LREE, whereas Sch-II largely falls in the area of vein-type W-Au deposits and spreads toward MREE. Additionally, the Y *vs* Ho plots diagram also indicates a vein-type (Au-)W deposit setting (Fig. 16b). Previous studies suggested that the scheelite from the Au-W deposits generally has similar chondrite-normalized REE patterns, which are characterized by flat to convex upward MREE-enrich pattern with a positive (or slightly negative) Eu anomaly (Poulin et al., 2016; Sciuba et al., 2020; Miranda et al., 2022), such as the Archean vein type gold deposits in the Kalgoorlie-Norseman region (Ghaderi et al., 1999; Australia), the Mt. Charlotte and Drysdale gold deposits (Brugger et al., 2000b; Australia), the Nova Scotia vein type gold deposit (Dostal et al. 2009; Canada) and the Bjorkdal intrusion-related gold deposit (Roberts et al., 2006; Sweden). The Sch-II in the Yangwuchang and Dashegou deposits are characterized by bell-shaped chondrite-normalized REE patterns with positive Eu anomalies that match with the scheelite from vein-type gold deposits. Thus, we suggest that Sch-II could be used to decipher the characteristics of Au mineralization.

As discussed above, redox-sensitive elements (Mo, Eu, and As) in the scheelite can indicate redox conditions. Compared to scheelite from other deposits, scheelite in the Yangwuchang and Dashegou deposits has an extremely low content of MoO_3 that indicates a strong reducing condition (Fig. 10). The positive Eu anomalies of scheelite also show a reducing environment ($Eu/Eu^* > 1$; Fig. 17). Arsenic, same as Mo and Eu, can incorporate into scheelite as As^{5+} under an oxidizing condition while reducing condition will inhibit it into scheelite as As^{2+} and As^{3+} (Poulin et al., 2018). In this study, most As concentrations of scheelite are below the detection line that points out a reduced ore-forming fluids system. In addition, co-existing chalcopyrite could infer a reduced mineralization environment as well (Fig. 5b and c; Liu et al., 2019). Therefore, we suggest that the Yangwuchang and Dashegou deposits are precipitated from a reduced fluid. The ore-forming fluids could be originated from the magmatic fluid, metamorphic fluid (e.g. the Yangxie gneiss suite Group), and the mixing of meteoric water (Sun and Chen, 2017; Yuan et al., 2019). Due to similar ionic radii and valence, element pairs like Y and Ho present extremely coherent geochemical behaviors. However, it will be decoupled by some geochemical processes like chemical complexation (Li et al., 2019). Hence, the positive correlation of Y and Ho can indicate that element behavior in this fluid system is mainly controlled by the function of charge and radius (Dostal et al., 2009; Li et al., 2019; Liu et al., 2019). In this study, the linear correlation between Y and Ho of two generations of scheelite suggests that they have a consistent ore-forming fluids source without significant differentiation (Fig. 16b).

Poulin et al. (2018) and Sciuba et al. (2020) used the chemical differences for Sr, Mo, and Eu anomaly in scheelite from different deposit types to determine the source of scheelite. As shown in Fig. 17, the metamorphic scheelite has low Mo content, high Sr/Mo ratio, and positive Eu anomaly. By contrast, the scheelite from magmatic hydrothermal settings shows high Mo content, low Sr/Mo ratio, and variable Eu anomaly. In this study, the plots of Sch-I and Sch-II come under the range of magmatic-hydrothermal setting and away from the metamorphic setting. Though some plots fall in the middle overlapping area of metamorphic and magmatic-hydrothermal settings. The plots generally show similar characteristics with the most scheelite from the magmatic-hydrothermal setting. Moreover, the W-Au mineralization in Early-Cretaceous in the Yangxie ore district is far later than the regional metamorphism event during subduction and collisional orogeny in the middle Palaeozoic, and thus excluded the possibility of metamorphic origin. In addition, S isotopes of sulfide minerals (pyrite and galena) in W(-Au)-bearing quartz veins have a narrow range of −4.67 to 2.25 ‰, indicating a uniform magmatic source (Wang, 1994). In addition, Yu (2017) based on the multi-analysis of the stable and noble isotope data in the Au-bearing quartz veins in the Yangxie ore district, including the C—H—O—S—Pb isotope analyses, suggested the ore-forming fluids and metals of the gold mineralization were also formed from a magmatic source. Hence, we infer that the ore-forming fluids of the Yangwuchang and Dashegou deposits were single-derived reduced magmatic fluids.

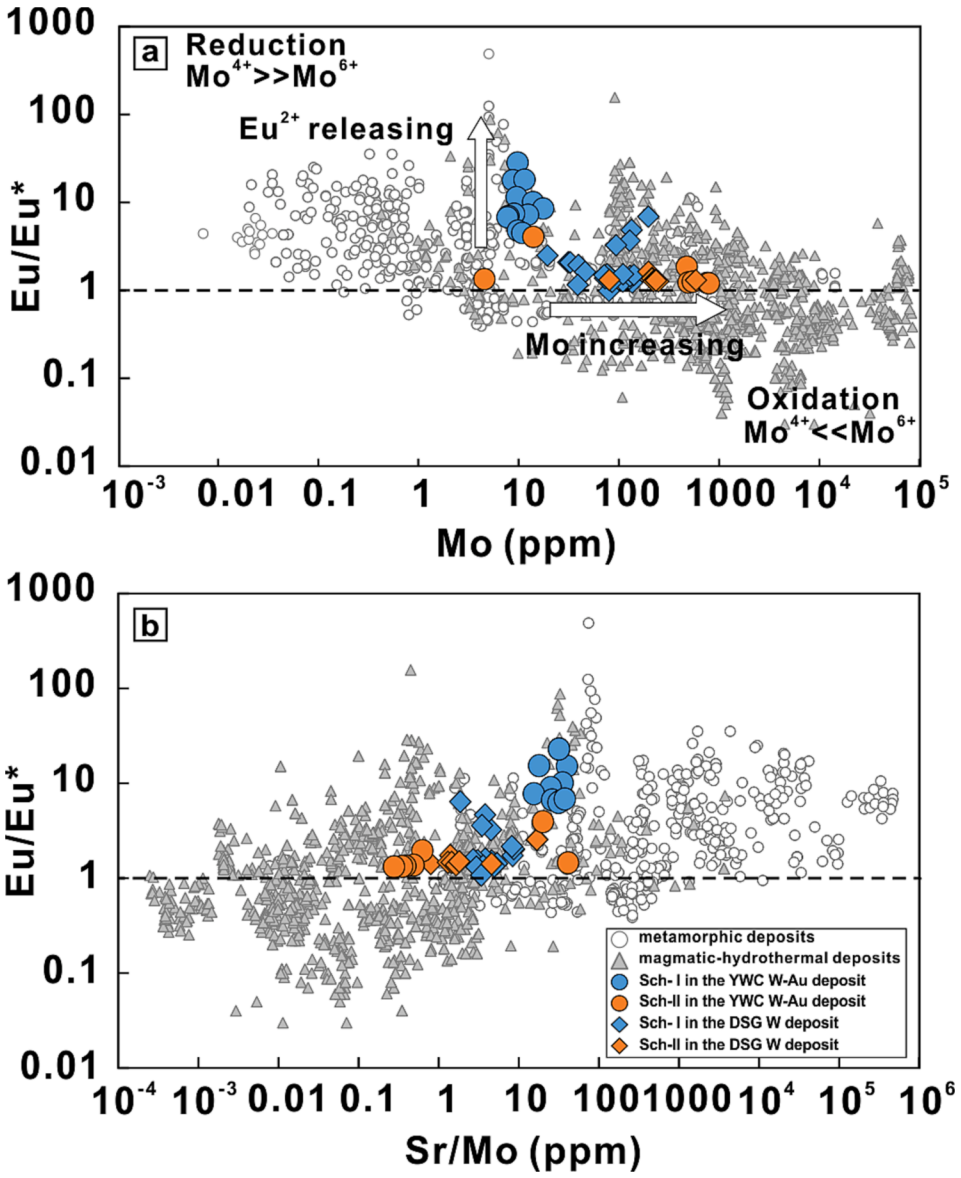

Fig. 17. (a) Scheelite plots of Eu/Eu* *vs* Mo (ppm). (b) Scheelite plots of Eu/Eu* *vs* Sr/Mo ratio. Data for scheelite from different metallogenic settings were collected from (Dostal et al., 2009; Poulin, 2016; Han et al., 2020; Liu et al., 2019; Song et al., 2019; Sun et al., 2019; Sciuba et al., 2020; Li et al., 2021; Zhan et al., 2021).

6.6. The ore-forming processes of the deposits

Previous studies invoked many possible mechanisms accounting for the W mineralization, such as the mixing of fluids (Li et al., 2018; Zhang et al., 2018), redox condition, fluid-rock interaction (Lecumberri-Sanchez et al., 2017; Liu et al., 2021b), fluid cooling (Wood and Samson, 2000), and pressure decrease (Korges et al., 2018; Liu et al., 2015). The mixing of magmatic fluids and meteoric water has been described as a possible controlling process for mineral precipitation, by changing the composition and physicochemical conditions of fluids (Vallance et al., 2001, Wei et al., 2012; Zhang et al., 2018). In addition, the redox state of hydrothermal fluid could control the metal association of deposits that gold mineralization is commonly associated with a reduced state (e.g. the Longshan Au-Sb-W deposit; Zhang et al., 2019), and oxidized condition generally related to the W-Mo association (e.g. the Sandaozhuang W-Mo deposit; Zhan et al., 2021). However, as we mentioned above, the ore-forming fluids in the Yangwuchang and Dashegou deposits were reduced (Fig. 10) and single-derived (Fig. 16b), precluding the mechanism of redox changing and fluids mixing, respectively. The extraction of ore-forming metals from country rocks by fluid-rock interaction has been proposed as an important role in W precipitation (Lecumberri-Sanchez et al., 2017; Sun et al., 2019). However, the host rock in the Yangxie ore district is deficient in Mn (~0.06 wt%) and W (~1 ppm) but sufficient in Ca (~2.7 wt%) and Fe (~4.3 wt%; Ge et al., 2021). Thus, if the host rock provided elements for mineralization, the Yangwuchang and Dashegou deposits will be mainly formed ferberite ($FeWO_4$) rather than hübnerite ($MnWO_4$) presented in the deposits. Hence, we suggest that the source of W and Mn should be derived from ore-forming magmatic fluids. In addition, a source of Ca is critical for scheelite mineralization. The host Yangxie gneiss Group contains abundant plagioclase (Ge et al., 2021). The alteration of plagioclase to sericite during greisenization provides significant amounts of Ca for scheelite precipitation (Heinrich, 1990; Zhang et al., 2018). Thus, the decomposition of plagioclase in the host rocks was decisive for the scheelite formation in the Yangwuchang and Dashegou deposits. Fluid inclusions studies revealed that pressure decrease of fluid during fracture opening in the vein system could trigger the precipitation of tungsten (Korges et al., 2018) and gold (Liu et al., 2015). It is suggested that scheelite is more soluble than wolframite under most W-mineralization conditions (Liu et al., 2021a). Hence, wolframite is easier to precipitate than

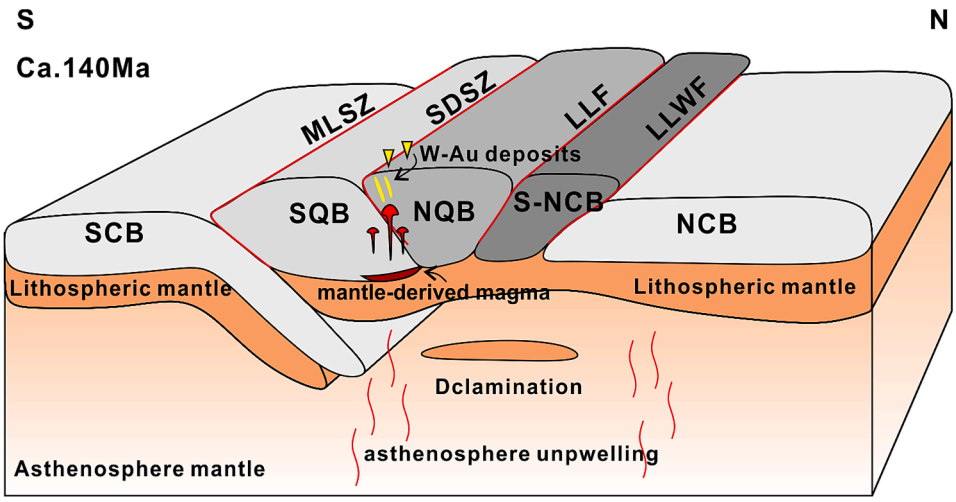

Fig. 18. A genetic model for the W-Au mineralization in the Yangwuchang and Dashegou deposits. S-NCB – Southern margin of the North China Block; NQB – the North Qinling Belt; SQB – the South Qinling Belt; *N*-SCB – Northern margin of the South China Block; LLWF – the Lingbao-Lushan -Wuyang Fault; LLF – the Luonan-Luanchuan Fault; SDSZ – the Shangdan Structure Zone; MLSZ – the Mianlue Structure Zone.

scheelite and a simple cooling of fluids is sufficient for precipitating wolframite from hydrothermal fluids (Wood and Samson, 2000). In addition, two mechanisms that can cause scheelite to replace wolframite are a temperature decrease with an increase ΣCa/ΣMn molality ratio or a pressure decrease (Liu et al., 2021a). In this study, the alteration of plagioclase provided external Ca which increases the ΣCa/ΣMn molality ratio in the ore-forming fluids. Hence, we speculate that fluid cooling and depressurization may be the most effective mechanism for W deposition in the Yangwuchang and Dashegou deposits.

Based on the multiple lines of evidence, the W-Au mineralization in the Yangwuchang and Dashegou deposits was genetically related to a W-Au-rich, reduced magmatic fluid in the Early Cretaceous. During Early-Cretaceous, the thinning of lithospheric and upwelling of the asthenosphere beneath the Qinling Orogen produced an extensional tectonic regime and intensive magmatic activities (Mao et al., 2008; Li et al., 2012; Zhao et al., 2018). This period of magmatic and mantle-derived fluids has contributed to the extensive mineralization of gold and tungsten in the East Qinling Orogenic Belt (Mao et al., 2011; Zhao et al., 2018), such as the Yangzhaiyu gold deposit (Li et al., 2021) and the Sandaozhuang W-Mo deposit (Zhan et al., 2021). Hence, the metallogenic model of the Yangwuchang W-Au deposit and Dashegou W deposit may have occurred as follows (Fig. 18). At ca.140 Ma, the lithospheric collapse and asthenosphere upwelling generated a magma which could provide fluids, metals (including W, Mn, Au, and REEs) and sulfur for the W-Au mineralization. The magma underwent continuous fractionation and evolution during migration and formed W-Au-rich reduced magmatic fluids. Then the magmatic fluids were released into the country rocks, ascended, and migrated along the fault structures in the ore district. The cooling and depressurization may lead to the precipitation of ore-forming elements during the migration of ore-forming fluids.

7. Conclusion

(1) The ages of wolframite directly restrict the timing of W mineralization is 141.8–139.1 Ma, which is consistent with the age of Au mineralization. The W-Au mineralization should be associated with Early-Cretaceous magmatism and exclude the possibility of collision orogeny mineralization in the Late-Triassic.
(2) Two generations of scheelite can be discriminated by CL features, Sch-I shows weak responses and oscillatory zonation patterns and Sch-II shows strong intensity and homogeneous patterns.
(3) $3Ca^{2+} = (2REE)^{3+} + \square Ca$ (site vacancy) is the main substitution mechanism of REEs into scheelite so that it could represent the REE features of the ore-forming fluids. The strong positive Eu anomalies were caused by the destruction of plagioclase of country rock during fluid-rock interaction and the weak positive Eu anomalies were inherited from the ore-forming fluid. The ore-forming fluids of the Yangwuchang W-Au deposit and Dashegou W deposit should be associated with a single-derived reduced magmatic fluid.
(4) The decomposition of plagioclase in the host rocks provided significant Ca for scheelite precipitation. Cooling and depressurization when the fluids ascended in the country rocks should be the main mechanism of W-Au mineralization.

Declaration of Competing Interest

The authors declare that they have no known competing financial interests or personal relationships that could have appeared to influence the work reported in this paper.

Data availability

Data will be made available on request.

Acknowledgments

The authors express great gratitude to Editor-in-Chief Prof. Huayong Chen and three anonymous reviewers for their constructive suggestions. For their guidance and assistance, we would like to thank the geologists of the Xi'an Center of Mineral Resources Survey, China Geological Survey, as well as Fengyuan Mining Development Co., Ltd for sampling permission and support. This research would not be possible without funds from the National Natural Science Foundation of China (Grant No. 42272095, 41730426, and 92062219), Overseas Expertise Introduction Project for Discipline Innovation (Grant No. BP0719021), Fundamental Research Funds for the Central Universities, China University of Geosciences (Grant No. 2652018164), and by MOST Special Fund from the State Key Laboratory of Geological Processes and Mineral Resources, China University of Geosciences.

Appendix A. Supplementary data

Supplementary data to this article can be found online at https://doi.

org/10.1016/j.oregeorev.2023.105359.

References

Bau, M., Möller, P., 1992. Rare earth element fractionation in metamorphogenic hydrothermal calcite, magnesite and siderite. Miner. Petrol. 45, 231–246. https://doi.org/10.1007/BF01163114.

Brugger, J., Bettiol, A., Costa, S., Lahaye, Y., Bateman, R., Lambert, D.D., Jamieson, D.N., 2000a. Mapping REE distribution in scheelite using luminescence. Mineral. Mag. 64, 891–903. https://doi.org/10.1180/002646100549724.

Brugger, J., Lahaye, Y., Costa, S., Lambert, D., Bateman, R., 2000b. Inhomogeneous distribution of REE in scheelite and dynamics of Archaean hydrothermal systems (Mt. Charlotte and Drysdale gold deposits, Western Australia). Contrib. Mineral. Petrol. 139, 251–264. https://doi.org/10.1007/s004100000135.

Brugger, J., Maas, R., Lahaye, Y., Mcrae, C., Ghaderi, M., Costa, S., Lambert, D., Bateman, R., Prince, K., 2002. Origins of Nd-Sr-Pb isotopic variations in single scheelite grains from Archaean gold deposits, Western Australia. Chem. Geol. 182, 203–225. https://doi.org/10.1016/S0009-2541(01)00290-X.

Burt, D., 1989. Compositional and phase relations among rare earth element minerals. Geochem. Mineral. Rare Earth Elements 21, 259–308. https://doi.org/10.1515/9781501509032-013.

Chen, Y.J., Li, C., Zhang, J., Li, Z., Wang, H.H., 2000. Sr and O isotopic characteristics of porphyries in the Qinling molybdenum deposit belt and their implication to genetic mechanism and type. Sci. China. Ser. D. 43, 82–94. https://doi.org/10.1007/BF02911935.

Chen, Y.J., Pirajno, F., Qi, J.P., Li, J., Wang, H.H., 2006. Ore geology, fluid geochemistry and genesis of the Shanggong gold deposit, Eastern Qinling Orogen, China. Resour. Geol. 56, 99–116. https://doi.org/10.1111/j.1751-3928.2006.tb00272.x.

Dai, Z.W., Li, G.M., Xie, Y.L., Yang, Z., Huizenga, J.M., Liang, W., Fu, J.G., Cao, H.W., 2022. Source and evolution of the ore-forming fluid of the Cuonadong Sn-W-Be polymetallic deposit (southern Tibet, China): Constraints from scheelite trace element and Sr isotope geochemistry. Ore Geol. Rev. 142, 104570 https://doi.org/10.1016/j.oregeorev.2021.104570.

Dai, H.Z., Wang, D.H., Liu, L.J., Huang, F., Wang, C.H., 2019. Metallogenic epoch and metallogenic model of the Hetaoping W-Be deposit in Zhen'an County, South Qinling. Acta Geol. Sin. 93, 1342–1358. https://doi.org/10.19762/j.cnki.dizhixuebao.2019158 (in Chinese with English abstract).

Deng, X.D., Luo, T., Li, J.W., Hu, Z.C., 2019. Direct dating of hydrothermal tungsten mineralization using in situ wolframite U-Pb chronology by laser ablation ICP-MS. Chem. Geol. 515, 94–104. https://doi.org/10.1016/j.chemgeo.2019.04.005.

Dickin, A.P., 2005. Radiogenic Isotope Geology, 2nd ed.,. Cambridge University Press, U. K, p. 509.

Dong, Y.P., Zhang, G.W., Neubauer, F., Liu, X.M., Genser, J., Hauzenberger, C., 2011. Tectonic evolution of the Qinling orogen, China: Review and synthesis. J. Asian Earth Sci. 41, 213–237. https://doi.org/10.1016/j.jseaes.2011.03.002.

Dostal, J., Kontak, D.J., Chatterjee, A., 2009. Trace element geochemistry of scheelite and rutile from metaturbidite-hosted quartz vein gold deposits, Meguma Terrane, Nova Scotia, Canada: genetic implications. Miner. Petrol. 97, 95. https://doi.org/10.1007/s00710-009-0067-0.

Frelinger, S.N., Ledvina, M.D., Kyle, J.R., Zhao, D., 2015. Scanning electron microscopy cathodoluminescence of quartz: Principles, techniques and applications in ore geology. Ore Geol. Rev. 65, 840–852. https://doi.org/10.1016/j.oregeorev.2014.10.008.

Fu, Y., Sun, X., Zhou, H., Lin, H., Jiang, L., Yang, T., 2017. In-situ LA-ICP-MS trace elements analysis of scheelites from the giant Beiya gold-polymetallic deposit in Yunnan Province, Southwest China and its metallogenic implications. Ore Geol. Rev. 80, 828–837. https://doi.org/10.1016/j.oregeorev.2016.08.030.

Ge, Z.L., Zheng, Y.R., Hao, D., Zhang, X.X., Li, X.D., Hua, L.P., Jing, Y.K., 2020. On the geological characteristics and genesis of Yangwuchang tungsten (gold) deposit in the Yangxie-Fengbeihe metallogenetic belt, East Qinling. Northwestern. Geology. 53, 140–152. https://doi.org/10.19751/j.cnki.61-1149/p.2020.03.012 (in Chinese with English abstract).

Ge, Z.L., Hao, D., Zhang, X.X., Zheng, Y.R., Li, X.D., Wu, H.W., Zhang, L., 2021. Petrogenesis of Host Rocks in the Dashegou Tungsten Orefield,East Qinling Orogen: Evidences from Zircon U-Pb Geochronology and Geochemistry. Geoscience. 35, 1633-1650 (in Chinese with English abstract). doi:10.19657/j.geoscience.1000-8527.2021.114.

Ghaderi, M., Palin, J.M., Campbell, I.H., Sylvester, P.J., 1999. Rare earth element systematics in scheelite from hydrothermal gold deposits in the Kalgoorlie-Norseman region, Western Australia. Econ Geol. 94, 423–437. https://doi.org/10.2113/gsecongeo.94.3.423.

Götze, J., 2002. Potential of cathodoluminescence (CL) microscopy and spectroscopy for the analysis of minerals and materials. Anal. Bioanal. Chem. 374, 703–708. https://doi.org/10.1007/s00216-002-1461-1.

Götze, J., Plötze, M., Habermann, D., 2001. Origin, spectral characteristics and practical applications of the cathodoluminescence (CL) of quartz-a review. Miner. Petrol. 71, 225–250. https://doi.org/10.1007/s007100170040.

Grasser, R., Pompe, W., Scharmann, A., 1988. Defect luminescence in tungstates. J. Lumines. 40, 343–344. https://doi.org/10.1016/0022-2313(88)90224-4.

Gu, X.X., Schulz, O., Vavtar, F., Liu, J.M., Zheng, M.H., Fu, S.H., 2007. Rare earth element geochemistry of the Woxi W-Sb-Au deposit, Hunan Province, South China. Ore Geol. Rev. 31, 319–336. https://doi.org/10.1016/j.oregeorev.2005.01.003.

Guo, Z.J., Li, J.W., Xu, X.Y., Song, Z.Y., Dong, X.Z., Tian, J., Yang, Y.C., She, H.Q., Xiang, A.P., Kang, Y.J., 2016. Sm-Nd dating and REE composition of scheelite for the Honghuaerji scheelite deposit, Inner Mongolia, Northeast China. Lithos 261, 307–321. https://doi.org/10.1016/j.lithos.2016.03.006.

Guo, Z.H., Zhang, B.L., Guo, B.W., Dang, Y.Q., Hou, J.L., 2018. Zircon U-Pb and Wolframite Sm-Nd Dating of the Bayinsukhtu Tungsten Deposit in Southern Mongolia and its Geological Significance. Resour. Geol. 68, 337–351. https://doi.org/10.1111/rge.12173.

Han, J.S., Chen, H.Y., Hong, W., Hollings, P., Chu, G., Zhang, L., Sun, S.Q., 2020. Texture and geochemistry of multi-stage hydrothermal scheelite in the Tongshankou porphyry-skarn Cu-Mo (-W) deposit, eastern China: Implications for ore-forming process and fluid metasomatism. Am. Miner. 105, 945–954. https://doi.org/10.2138/am-2020-7194.

Han, K., Ke, Y.X., Chao, H.X., He, H.J., Ruan, S.Q., Gao, Y.F., Zhang, W.S., Zhu, W., Jin, G., 2021. U-Pb Zircon and Re-Os Molybdenite Geochronology of the W-Mo Mineralized Region of South Qinling, China, their Tectonic Implications. Acta Geol. Sin. Engl. Ed. 95, 500–516. https://doi.org/10.1111/1755-6724.14653.

Heinrich, C.A., 1990. The chemistry of hydrothermal tin(-tungsten) ore deposition. Econ. Geol. 85, 457–481. https://doi.org/10.2113/gsecongeo.85.3.457.

Hu, F.Y., Liu, S.W., Zhang, W.Y., Deng, Z.B., Chen, X., 2016. A westward propagating slab tear model for Late Triassic Qinling Orogenic Belt geodynamic evolution: Insights from the petrogenesis of the Caoping and Shahewan intrusions, central China. Lithos 262, 486–506. https://doi.org/10.1016/j.lithos.2016.07.034.

Hu, Z.C., Zhang, W., Liu, Y.S., Gao, S., Li, M., Zong, K.Q., Chen, H.H., Hu, S.H., 2015. "Wave" signal-smoothing and mercury-removing device for laser ablation quadrupole and multiple collector ICPMS analysis: application to lead isotope analysis. Anal. Chem. 87, 1152–1157. https://doi.org/10.1021/ac503749k.

Korges, M., Weis, P., Lüders, V., Laurent, O., 2018. Depressurization and boiling of a single magmatic fluid as a mechanism for tin-tungsten deposit formation. Geology 46, 75–78. https://doi.org/10.1130/G39601.1.

Kovalenker, V., Plotinskaya, O.Y., Kiseleva, G., Minervina, E., Borisovskii, S., Zhilicheva, O., Yazykova, Y.I., 2019. Scheelite of the bystrinskoe skarn-porphyry Cu–Au–Fe deposit, eastern transbaikal region, russia: genetic implications. Geol. Ore Deposits 61, 559–579. https://doi.org/10.1134/S1075701519060035.

Kwak, T.A.P., Tan, T.H., 1981. The geochemistry of zoning in skarn minerals at the King Island (Dolphin) Mine. Econ. Geol. 76, 468–497. https://doi.org/10.2113/gsecongeo.76.2.468.

Lecumberri-Sanchez, P., Vieira, R., Heinrich, C.A., Pinto, F., Walle, M., 2017. Fluid-rock interaction is decisive for the formation of tungsten deposits. Geology 45, 579–582. https://doi.org/10.1130/G38974.1.

Lei, X.F., Jiang, S.Y., Su, H.M., Ying, Y.C., 2021. Hydrothermal titanite U-Pb age and geochemistry as a reliable chronometer and genetic tracer for quartz vein-type tungsten deposit at Qipangou of Qinling orogenic belt, Central China. Ore Geol. Rev. 135, 104246 https://doi.org/10.1016/j.oregeorev.2021.104246.

Lenz, C., Nasdala, L., 2015. A photoluminescence study of REE3+ emissions in radiation-damaged zircon. Am. Miner. 100, 1123–1133. https://doi.org/10.2138/am-2015-4894ccbyncnd.

Li, N., Chen, Y.J., Pirajno, F., Ni, Z.Y., 2013. Timing of the Yuchiling giant porphyry Mo system, implications for ore genesis. Miner. Deposita 48, 505–524. https://doi.org/10.1007/s00126-012-0441-4.

Li, X.Y., Gao, J.F., Zhang, R.Q., Lu, J.J., Chen, W.H., Wu, J.W., 2018. Origin of the Muguayuan veinlet-disseminated tungsten deposit, South China: Constraints from in-situ trace element analyses of scheelite. Ore Geol. Rev. 99, 180–194. https://doi.org/10.1016/j.oregeorev.2018.06.005.

Li, J.W., Li, Z.K., Zhou, M.F., Chen, L., Bi, S.J., Deng, X.D., Qiu, H.N., Cohen, B., Selby, D., Zhao, X.F., 2012. The Early Cretaceous Yangzhaiyu lode gold deposit, North China Craton: a link between craton reactivation and gold veining. Econ. Geol. 107, 43–79. https://doi.org/10.2113/econgeo.107.1.43.

Li, J.D., Li, X.F., Xiao, R., 2019. Multiple-stage tungsten mineralization in the Silurian Jiepai W skarn deposit, South China: Insights from cathodoluminescence images, trace elements, and fluid inclusions of scheelite. J. Asian Earth Sci. 181, 103898 https://doi.org/10.1016/j.jseaes.2019.103898.

Li, W.S., Ni, P., Pan, J.Y., De Vivo, B., Albanese, S., Fan, M.S., Gao, Y., Zhang, D.X., Chi, Z., 2022. Co-genetic formation of scheelite-and wolframite-bearing quartz veins in the Chuankou W deposit, South China: Evidence from individual fluid inclusion and wall-rock alteration analysis. Ore Geol. Rev. 142, 104723 https://doi.org/10.1016/j.oregeorev.2022.104723.

Li, W., Xie, G.Q., Cook, N.J., Mao, J.W., Li, C., Ciobanu, C.L., Zhang, Z.Y., 2021. Tracking dynamic hydrothermal processes: Textures, in-situ Sr-Nd isotopes, trace-element analysis of scheelite from the Yangjiashan vein-type W deposit, South China. Am. Miner. 106, 1987–2002. https://doi.org/10.2138/am-2021-7677.

Linnen, R.L., Williams-Jones, A.E., 1990. Evolution of aqueous-carbonic fluids during contact metamorphism, wall-rock alteration, molybdenite deposition at Trout Lake, British Columbia. Econ. Geol. 85, 1840–1856. https://doi.org/10.2113/gsecongeo.85.8.1840.

Liu, Q., 2013. The Characteristics and Genes's of the Zhen'an W deposit, ShanXi Province, China. China University of Geosicences, Beijing. Ms thesis.

Liu, J.J., Dai, H.Z., Zhai, D.G., Wang, J.P., Wang, Y.H., Yang, L.B., Mao, G.J., Liu, X.H., Liao, Y.F., Yu, C., 2015. Geological and geochemical characteristics and formation mechanisms of the Zhaishang Carlin-like type gold deposit, western Qinling Mountains, China. Ore Geol. Rev. 64, 273–298. https://doi.org/10.1016/j.oregeorev.2014.07.016.

Liu, Z.K., Hollings, P., Mao, X.C., Lawley, C.J.M., Yang, B., Tang, L., 2021b. Metal remobilization from country rocks into the Jiaodong-type orogenic gold systems, Eastern China: New constraints from scheelite and galena isotope results at the Xiadian and Majiayao gold deposits. Ore Geol. Rev. 134, 104126 https://doi.org/10.1016/j.oregeorev.2021.104126.

Liu, Y.S., Hu, Z.C., Gao, S., Günther, D., Xu, J., Gao, C.G., Chen, H.H., 2008. In situ analysis of major and trace elements of anhydrous minerals by LA-ICP-MS without applying an internal standard. Chem. Geol. 257, 34–43. https://doi.org/10.1016/j.chemgeo.2008.08.004.

Liu, B., Li, H., Wu, Q.H., Evans, N.J., Cao, J.Y., Jiang, J.B., Wu, J.H., 2019. Fluid evolution of Triassic and Jurassic W mineralization in the Xitian ore field, South China: Constraints from scheelite geochemistry and microthermometry. Lithos 330, 1–15. https://doi.org/10.1016/j.lithos.2019.02.003.

Liu, X.C., Xiao, C.H., Wang, Y., 2021a. The relative solubilities of wolframite and scheelite in hydrothermal fluids: Insights from thermodynamic modeling. Chem. Geol. 584, 120488. https://10.1016/j.chemgeo.2021.120488.

Liu, X.X., Zhang, J., Huang, F., Cheng, J.W., Lu, K.X., Yang, J.F., Wang, M., Wang, Y.X., Qiu, J.W., Zhang, X.Y., 2022. Tungsten deposits in southern Jiangxi Province: Constraints on the origin of wolframite from in-situ U-Pb isotope dating. Ore Geol. Rev. 143, 104774. https://doi.org/10.1016/j.oregeorev.2022.104774.

Ludwig, K.R., 2003. User's manual for IsoPlot 3.0, a geochronological toolkit for Microsoft Excel. Berkeley Geochronl Cent Spec Publ. 4 (2003), 25–32.

Macrae, C.M., Wilson, N.C., Brugger, J., 2009. Quantitative cathodoluminescence mapping with application to a Kalgoorlie scheelite. Microsc Microanal. 15, 222–230. https://doi.org/10.1017/S1431927609090308.

Mao, J.W., Xie, G.Q., Zhang, Z.H., Li, X.F., Wang, Y.T., Zhang, C.Q., Li, Y.F., 2005. Mesozoic large-scale metallogenic pulses in North China and corresponding geodynamic settings. Acta Geol. Sin. 21, 169–188 (in Chinese with English abstract).

Mao, J.W., Xie, G.Q., Bierlein, F., Qü, W.J., Du, A.D., Ye, H.S., Pirajno, F., Li, H.M., Guo, B.J., Li, Y.F., Yang, Z.Q., 2008. Tectonic implications from Re-Os dating of Mesozoic molybdenum deposits in the East Qinling-Dabie orogenic belt. Geochim. Cosmochim. Acta 72, 4607–4626. https://doi.org/10.1016/j.gca.2008.06.027.

Mao, J.W., Pirajno, F., Xiang, J.F., Gao, J.J., Ye, H.S., Li, Y.F., Guo, B.J., 2011. Mesozoic molybdenum deposits in the east Qinling-Dabie orogenic belt: characteristics and tectonic settings. Ore Geol. Rev. 43, 264–293. https://doi.org/10.1016/j.oregeorev.2011.07.009.

Meng, Q.R., Zhang, G.W., 1999. Timing of collision of the North and South China blocks; controversy and reconciliation. Geology 27, 123–126. https://doi.org/10.1130/0091-7613(1999)027<0123:TOCOTN>2.3.CO;2.

Miranda, A.C.R., Beaudoin, G., Rottier, B., 2022. Scheelite chemistry from skarn systems: implications for ore-forming processes and mineral exploration. Miner. Deposita 2022, 1–29. https://doi.org/10.1007/s00126-022-01118-y.

Müller, A., Herrington, R., Armstrong, R., Seltmann, R., Kirwin, D.J., Stenina, N.G., Kronz, A., 2010. Trace elements and cathodoluminescence of quartz in stockwork veins of Mongolian porphyry-style deposits. Miner. Deposita 45, 707–727. https://doi.org/10.1007/s00126-010-0302-y.

Nassau, K., Loiacono, G., 1963. Calcium tungstate-III: trivalent rare earth substitution. J. Phys. Chem. Solids 24, 1503–1510. https://doi.org/10.1016/0038-1098(63)90059-0.

Neto, J.A.S., Legrand, J.M., Volfinger, M., Pascal, M.L., Sonnet, P., 2008. W-Au skarns in the Neo-Proterozoic Seridó Mobile Belt, Borborema Province in northeastern Brazil: an overview with emphasis on the Bonfim deposit. Miner Deposita. 43, 185–205. https://doi.org/10.1007/s00126-007-0155-1.

Pan, J.Q., Dai, T.G., Zhang, D.X., Li, W.H., Bayless, R.C., Gao, J.F., 2020. In Situ Trace Elemental Analyses of Scheelite from the Chuankou Deposit, South China: Implications for Ore Genesis. Minerals 10, 1007. https://doi.org/10.3390/min10111007.

Poulin, R.S., 2016. A study of the crystal chemistry, cathodoluminescence, geochemistry and oxygen isotopes in Scheelite: application towards discriminating among differing ore-deposit systems. Laurentian University of Sudbury. Ph.D. thesis.

Poulin, R.S., Mcdonald, A.M., Kontak, D.J., Mcclenaghan, M.B., 2016. On the relationship between cathodoluminescence and the chemical composition of scheelite from geologically diverse ore-deposit environments. Can. Mineral. 54, 1147–1173. https://doi.org/10.3749/canmin.1500023.

Poulin, R.S., Kontak, D.J., Mcdonald, A., Mcclenaghan, M.B., 2018. Assessing scheelite as an ore-deposit discriminator using its trace-element and REE chemistry. Can. Mineral. 56, 265–302. https://doi.org/10.3749/canmin.1500023.

Qin, J.H., Wang, D.H., Li, C., Chen, Y.C., Cai, F.C., 2020. The molybdenite Re-Os isotope chronology, in situ scheelite and wolframite trace elements and Sr isotope characteristics of the Chuankou tungsten ore field, South China. Ore Geol. Rev. 126, 103756 https://doi.org/10.1016/j.oregeorev.2020.103756.

Rempel, K.U., Williams-Jones, A.E., Migdisov, A.A., 2009. The partitioning of molybdenum (VI) between aqueous liquid and vapour at temperatures up to 370 C. Geochim. Cosmochim. Acta 73, 3381–3392. https://doi.org/10.1016/j.gca.2009.03.004.

Roberts, S., Palmer, M.R., Waller, L., 2006. Sm-Nd and REE Characteristics of Tourmaline and Scheelite from the Bjǒrkdal Gold Deposit, Northern Sweden: Evidence of an Intrusion-Related Gold Deposit? Econ. Geol. 101, 1415–1425. https://doi.org/10.2113/gsecongeo.101.7.1415.

Rusk, B.G., 2012. Cathodoluminescent textures and trace elements in hydrothermal quartz. Quartz: deposits, mineralogy and analytics. Springer, Berlin, Heidelberg, pp. 307–329.

Sciuba, M., Beaudoin, G., Grzela, D., Makvandi, S., 2020. Trace element composition of scheelite in orogenic gold deposits. Miner Deposita. 55, 1149–1172. https://doi.org/10.1007/s00126-019-00913-4.

Shannon, R.D., 1976. Revised effective ionic radii and systematic studies of interatomic distances in halides and chalcogenides. Acta Crystallogr Sect A 32, 751–767. https://doi.org/10.1107/S0567739476001551.

Song, G.X., Qin, K.Z., Li, G.M., Evans, N.J., Chen, L., 2014. Scheelite elemental and isotopic signatures: Implications for the genesis of skarn-type W-Mo deposits in the Chizhou Area, Anhui Province, Eastern China. Am. Miner. 99, 303–317. https://doi.org/10.2138/am.2014.4431.

Song, G.X., Cook, N.J., Li, G.M., 2019. Scheelite geochemistry in porphyry-skarn W-Mo systems: A case study from the Gaojiabang Deposit, East China. Ore Geol. Rev. 113, 103084 https://doi.org/10.1016/j.oregeorev.2019.103084.

Su, S.Q., Qin, K.Z., Li, G.M., Olin, P., Thompson, J., 2019. Cathodoluminescence and trace elements of scheelite: Constraints on ore-forming processes of the Dabaoshan porphyry Mo-W deposit, South China. Ore Geol. Rev. 115, 103183 https://doi.org/10.1016/j.oregeorev.2019.103183.

Sun, K.K., Chen, B., 2017. Trace elements and Sr-Nd isotopes of scheelite: Implications for the W-Cu-Mo polymetallic mineralization of the Shimensi deposit, South China. Am. Miner. 102, 1114–1128. https://doi.org/10.2138/am-2017-5654.

Sun, K.K., Chen, B., Deng, J., 2019. Ore genesis of the Zhuxi supergiant W-Cu skarn polymetallic deposit, South China: Evidence from scheelite geochemistry. Ore Geol. Rev. 107, 14–29. https://doi.org/10.1016/j.oregeorev.2019.02.017.

Sun, S.S., McDonough, W.F., 1989. Chemical and isotopic systematics of oceanic basalts: implications for mantle composition and processes. Geol. Soc. Lond., Spec. Publ. 42, 313–345. https://doi.org/10.1144/GSL.SP.1989.042.01.19.

Tang, Y.W., Cui, K., Zheng, Z., Gao, J.F., Han, J.J., Yang, J.H., Liu, L., 2020. LA-ICP-MS U Pb geochronology of wolframite by combining NIST series and common lead-bearing MTM as the primary reference material: Implications for metallogenesis of South China. Gondwana Res. 83, 217–231. https://doi.org/10.1016/j.gr.2020.02.006.

Vallance, J., Cathelineau, M., Marignac, C., Boiron, M.C., Fourcade, S., Martineau, F., Fabre, C., 2001. Microfracturing and fluid mixing in granites: W-(Sn) ore deposition at Vaulry (NW French Massif Central). Tectonophysics 336, 43–61. https://doi.org/10.1016/S0040-1951(01)00093-2.

Wang, Z.Q., 1994. The geochemistry characteristics and genetic analysis for W-Au deposit in Yangxie, Shangzhou. Geology of Shaanxi 12, 14–21.

Wang, Y.Y., Van Den Kerkhof, A., Xiao, Y.L., Sun, H., Yang, X.Y., Lai, J.Q., Wang, Y.G., 2017. Geochemistry and fluid inclusions of scheelite-mineralized granodiorite porphyries from southern Anhui Province, China. Ore Geol. Rev. 89, 988–1005. https://doi.org/10.1016/j.oregeorev.2017.08.004.

Wang, M.F., Zhao, R.Z., Shang, X.Y., Wei, K.T., Liu, K., An, W.W., 2022. REE and cathodoluminescence features of scheelites from the Tongshankou Cu–Mo deposit in Eastern China. Ore Geol. Rev. 147, 104998 https://doi.org/10.1016/j.oregeorev.2022.104998.

Wei, W.F., Hu, R.Z., Bi, X.W., Peng, J.T., Su, W.C., Song, S.Q., Shi, S.H., 2012. Infrared microthermometric and stable isotopic study of fluid inclusions in wolframite at the Xihuashan tungsten deposit, Jiangxi province, China. Miner. Deposita 47, 589–605. https://doi.org/10.1007/s00126-011-0377-0.

Wood, S.A., Samson, I.M., 2000. The hydrothermal geochemistry of tungsten in granitoid environments: I. Relative solubilities of ferberite and scheelite as a function of T, P, pH, and mNaCl. Econ. Geol. 95, 143–182. https://doi.org/10.2113/gsecongeo.95.1.143.

Wu, Y.F., Li, J.W., Evans, K., Fougerouse, D., Rempel, K., 2019. Source and possible tectonic driver for Jurassic-Cretaceous gold deposits in the West Qinling Orogen, China. Geosci. Front. 10, 107–117. https://doi.org/10.1016/j.gsf.2018.09.005.

Xiao, X., Zhou, T., Shi, K., White, N.C., Fan, Y., Wang, F., Chen, X., 2022. Trace elements and textures of scheelite in porphyry-skarn Cu-Au systems: The example of Dongguashan deposit, eastern China. Ore Geol. Rev. 105069 https://doi.org/10.1016/j.oregeorev.2022.105069.

Yang, M., Yang, Y.H., Wu, S.T., Romer, R.L., Che, X.D., Zhao, Z.F., Li, W.S., Yang, J.H., Wu, F.Y., Xie, L.W., Huang, C., Zhang, D., Zhang, Y., 2020. Accurate and precise in situ U-Pb isotope dating of wolframite series minerals via LA-SF-ICP-MS. J. Anal. At Spectrom. 35, 2191–2203. https://doi.org/10.1039/D0JA00248H.

Yin, C., Liu, J.J., Carranza, E.J.M., 2019. Mineralogical constraints on the genesis of the Dahu quartz vein-style Au-Mo deposit, Xiaoqinling gold district, China: Implications for phase relationships and physicochemical conditions. Ore Geol. Rev. 113, 107. https://doi.org/10.1016/j.oregeorev.2019.103107.

Yu, X.H., 2017. Mineralization characteristics and Genesis of the Yangxie Gold Deposit in the North Qinling Belt. China University of Geosciences, Beijing. Ms thesis.

Yuan, S.D., Williams-Jones, A.E., Mao, J.W., Zhao, P.L., Yan, C., Zhang, D.L., 2018. The origin of the Zhangjialong tungsten deposit, South China: Implications for W-Sn mineralization in large granite batholiths. Econ. Geol. 113, 1193–1208. https://doi.org/10.5382/econgeo.2018.4587.

Yuan, S.D., Williams-Jones, A.E., Romer, R.L., Zhao, P., Mao, J.W., 2019. Protolith-related thermal controls on the decoupling of Sn and W in Sn-W metallogenic provinces: Insights from the Nanling region, China. Econ. Geol. 114, 1005–1012. https://doi.org/10.5382/econgeo.4669.

Zaw, K., Singoyi, B., 2000. Formation of magnetite-scheelite skarn mineralization at Kara, northwestern Tasmania: evidence from mineral chemistry and stable isotopes. Econ. Geol. 95, 1215–1230. https://doi.org/10.2113/gsecongeo.95.6.1215.

Zhan, Q., Gao, X.Y., Meng, L., Zhao, T.P., 2021. Ore genesis and fluid evolution of the Sandaozhuang supergiant W-Mo skarn deposit, southern margin of the North China Craton: Insights from scheelite, garnet and clinopyroxene geochemistry. Ore Geol. Rev. 139, 104551 https://doi.org/10.1016/j.oregeorev.2021.104551.

Zhang, Y.H., 2014. Late-Mesozoic tectonic-magma evolution and its relationship with mineralization in Luanchuan County. China University of Geosciences, Beijing. Ms thesis.

Zhang, Y., Ma, D.S., Gao, J.F., 2020. Origin and evolution of ore-forming fluids in a tungsten mineralization system, Middle Jiangnan orogenic belt, South China: Constraints from in-situ LA-ICP-MS analyses of scheelite. Ore Geol. Rev. 127, 103806 https://doi.org/10.1016/j.oregeorev.2020.103806.

Zhang, G.W., Meng, Q.G., Lai, S.C., 1995. Tectonics and structure of Qinling orogenic belt. Sci. China Ser. B 38, 1379–1394 (in Chinese with English abstract).

Zhang, Z.Y., Xie, G.Q., Mao, J.W., Liu, W., Olin, P., Li, W., 2019. Sm-Nd dating and in-situ LA-ICP-MS trace element analyses of scheelite from the Longshan Sb-Au deposit, Xiangzhong metallogenic province, south China. Minerals 9, 87. https://doi.org/10.3390/min9020087.

Zhang, Y.H., Zhang, S.T., Xu, M., Jiang, X.K., Li, J.J., Wang, S.Y., Li, D., Cao, H.W., Zou, H., Fang, Y., 2015. Geochronology, geochemistry, Hf isotopes of the Jiudinggou molybdenum deposit, Central China, their geological significance. Geochem. J. 49, 321–342. https://doi.org/10.2343/geochemj.2.0359.

Zhang, Q., Zhang, R.Q., Gao, J.F., Lu, J.J., Wu, J.W., 2018. In-situ LA-ICP-MS trace element analyses of scheelite and wolframite: Constraints on the genesis of veinlet-disseminated and vein-type tungsten deposits, South China. Ore Geol. Rev. 99, 166–179. https://doi.org/10.1016/j.oregeorev.2018.06.004.

Zhao, T.P., Meng, L., Gao, X.Y., Jin, C., Wu, Q., Bao, Z.W., 2018. Late Mesozoic felsic magmatism and Mo-Au-Pb-Zn mineralization in the southern margin of the North China Craton: A review. J. Asian Earth Sci. 161, 103–121. https://doi.org/10.1016/j.jseaes.2018.04.020.

Zhou, T.C., Zeng, Q.D., Gao, S., Chu, S.X., Yang, J.H., 2020. Geochronology, geochemistry and fluid inclusions of the Yechangping giant porphyry-skarn Mo-W deposit, East Qinling, China. Ore Geol. Rev. 127, 103823 https://doi.org/10.1016/j.oregeorev.2020.103823.

Zhu, L.M., Zhang, G.W., Guo, B., Lee, B., Gong, H.J., Wang, F., 2010. Geochemistry of the Jinduicheng Mo-bearing porphyry and deposit, its implications for the geodynamic setting in East Qinling, PR China. Geochemistry. 70, 159–174. https://doi.org/10.1016/j.chemer.2009.12.003.